PAPER

Spanwise phase transition between pure modes A and B in a circular cylinder's wake. Part II: spatiotemporal evolution of vorticity

IOP Publishing | The Japan Society of Fluid Mechanics Fluid Dynamics Research
Fluid Dyn. Res. **55** (2023) 055505 (36pp) https://doi.org/10.1088/1873-7005/ad02ba

Spanwise phase transition between pure modes A and B in a circular cylinder's wake. Part II: spatiotemporal evolution of vorticity

L M Lin

Key Laboratory for Mechanics in Fluid Solid Coupling Systems, Institute of Mechanics, Chinese Academy of Sciences, Beijing 100190, People's Republic of China

E-mail: llmbirthday@163.com

Received 28 April 2023; revised 2 October 2023
Accepted for publication 12 October 2023
Published 24 October 2023

Communicated by Professor Hyung Jin Sung

Abstract

Through direct numerical simulation, the transition from pure mode A to mode B in the near wake of a circular cylinder is studied without consideration of vortex dislocations. The Reynolds number Re is calculated from 100 to 330 with a computational spanwise length of 4 diameters. In the present section, the spatiotemporal evolution of the vorticity and its sign are analyzed. The results show that mode B, as a kind of weak disturbed vorticity with opposite signs, actually appears partially on the rear surface of the cylinder and in the shear layers once Re exceeds 193. With increasing Re, the vortex-shedding patterns in the near wake undergo the initial generation stage of mode B coupling with the fully developed pure mode A ($193 \leqslant Re < 230$), the mode swapping or coexistence stage between modes A and B ($230 \leqslant \mathrm{Re} < 260 \sim 265$), the self-adjustment stage of the nondimensional spanwise wavelength from 0.8 to 1 in dominant mode B ($260 \sim 265 \leqslant \mathrm{Re} < 310$), and the full development stage of mode B ($\mathrm{Re} \geqslant 310$). In particular, the spanwise phase transition initially occurs at a certain spanwise position in the initial generation stage where a part of mode A and a part of mode B with specific vorticity signs appear, e.g. the Π_- vortex in mode A and the Π_+ vortex in mode B, in which Π_- and Π_+ vortices are vortices with three vorticity components satisfying the vorticity sign law and shed from the upper and lower shear layers, respectively.

Keywords: spanwise phase transition, wake, circular cylinder, mode A, mode B

1. Introduction

A bluff body is widely implemented in many engineering applications, such as suspension bridges, high architectures, flexible risers and heat exchangers. Fluid flow past a bluff body is a classical and basic subject in fluid mechanics. One main reason for this interest is the appearance of unsteady wake associated with vortices alternately shedding behind a body. As a result, large unsteady fluid forces act on a body, which has the potential to cause fatigue damage and even destroy the structural integrity. Toward understanding and controlling wake vortex dynamics, many studies (Karniadakis and Triantafyllou 1992, Wu and Ling 1993, Barkley and Henderson 1996, Williamson 1996a, 1996b, Henderson 1997, Prasad and Williamson 1997, Leweke and Williamson 1998, Persillon and Braza 1998, Ling and Chang 1999, Barkley *et al* 2000, Darekar and Sherwin 2001, Posdziech and Grundmann 2001, Thompson *et al* 2001, Sheard *et al* 2003, Rao *et al* 2013, Jiang *et al* 2016, 2017, 2018, Agbaglah and Mavriplis 2017, 2019, Jiang and Cheng 2019) have been published in recent decades that apply analysis any methods, including physical model testing, direct numerical simulations (DNSs), and linear or nonlinear stability analysis. Comprehensive reviews can be found in previous references (Williamson 1996a, Posdziech and Grundmann 2001).

As a typical example of such a problem considering flow past a circular cylinder, four laminar stages for different flow structures in the wake mainly appear in a wake transition sequence (Williamson 1996a). In the laminar steady regime at a Reynolds number Re below approximately 49, where Re is defined based on the approaching flow velocity U_∞, the cylinder diameter D and the kinematic viscosity ν of the fluid, the wake comprises a steady recirculation region of two symmetrically placed vortices on each side of the wake. After the primary wake instability emerges at $\mathrm{Re} > 49$ due to a Hopf bifurcation, the two-dimensional (2D) spanwise vortices (with spanwise vorticity ω_z) are alternately shed from the body, known as Kármán vortex streets, in the laminar vortex shedding regime at $\mathrm{Re} < 140 \sim 194$. Until Re reaches approximately 260, two discontinuous changes, mainly associated with two wake instabilities, i.e. modes A and B, in the wake formation appear in the three-dimensional (3D) laminar wake transition regime. Beyond a Reynolds number of 260 in the last stage, a particularly ordered 3D streamwise vortex structure (with streamwise vorticity ω_x) in the near wake, as the fine-scale three dimensionality, becomes increasingly disordered, and the primary wake instability behaves remarkably like the laminar shedding mode.

In particular, in the 3D laminar wake-transition regime, two different wake instabilities appear successively with their specific mechanisms and features, typically manifested by the variation of Strouhal number St (nondimensional vortex-shedding frequency) as Re increases (Williamson 1996a, Leweke and Williamson 1998, Ling and Chang 1999, Thompson *et al* 2001, Jiang *et al* 2016). At the first discontinuity which is hysteretic near $\mathrm{Re} = 180 \sim 194$, the first wake instability, i.e. (pure) mode A, occurs with the inception of vortex loops due to the spanwise wavy deformation of primary vortices as they are shed. Such deformation is caused by an elliptic instability of the primary vortex cores and the formation of streamwise vortex pairs at a spanwise wavelength of approximately $3 \sim 4$ diameters results from Biot-Savart induction. At the second discontinuous change in the $\mathrm{St} - \mathrm{Re}$ relation over a range of Re from 230 to 250, the second wake instability, i.e. (pure) mode B, gradually appears due to a gradual transfer of energy from mode A shedding. Such mode B comprises finer-scale streamwise vortices, with a spanwise length scale of approximately one diameter. This occurs mainly due to a hyperbolic instability of the braid shear layer region. In addition, there are other formation mechanisms (Yokoi and Kamemoto 1992, 1993, Brede *et al* 1996, Agbaglah and

Mavriplis 2017, Lin and Tan 2019, 2022, Lin *et al* 2019b, Kokash and Agbaglah 2022), such as vortex tongues under an instability of the braid region (Brede *et al* 1996), axial stretching of the upstream perturbed vorticity (Agbaglah and Mavriplis 2017) and 3D instability on and near the cylinder surface coupling with the vortex-induced vortex mechanism (Lin and Tan 2019, Lin *et al* 2019b, Lin 2022) in mode A.

Aside from the above two pure modes, there is a large intermittent low-frequency wake velocity fluctuation owing to the presence of large-scale spot-like vortex dislocations in the wake transition from mode A, i.e. mode A* (mode A + vortex dislocations) (Williamson 1996a). The critical Reynolds number Re_{cr} at which mode A* wake instability emerges is identified at 194 in certain experiments, for which the end effects are eliminated by using nonmechanical end conditions (Williamson 1996b). This value is very close to those of 188.5 ($\pm$1.0), 190 ($\pm$0.02) and 190.5 predicted through linear stability analysis (Barkley and Henderson 1996, Posdziech and Grundmann 2001, Rao *et al* 2013), and 194 and 195 (at most) calculated by DNS (Jiang *et al* 2016, Lin 2022). In addition, the effect of mode A* instability destabilizes mode B in the nonlinear interaction between the two modes (Henderson 1997). These dynamics lead to the first emergence of mode B instability at Re $\sim$ 230 in experiments (Williamson 1996b) much lower than the critical Re of 259 and 261 ($\pm$0.2) predicted through linear stability analysis (Barkley and Henderson 1996, Posdziech and Grundmann 2001), but in good agreement with the predicted Re = 230 based on nonlinear stability analysis (Barkley *et al* 2000, Sheard *et al* 2003). Moreover, experimental study has revealed that the wake transition from mode A* to mode B is a gradual process with intermittent swapping between the two modes (Williamson 1996b). Therefore, the appearance of mode A* or vortex dislocations will significantly interfere with both pure modes A and B in the 3D wake transition of a circular cylinder. It should be stated that the concept of 'pure' modes A and B in this paper refers to vortex-shedding patterns that satisfy the spatiotemporal symmetry of vorticity in the near wake (Barkley and Henderson 1996, Robichaux *et al* 1999) and specific spanwise wavelengths above in modes A and B, respectively, without any interference, such as vortex dislocations.

Correspondingly, the question arises: are vortex dislocations an indispensable condition in the transition from mode A to mode B? In other words, when the phenomenon of vortex dislocations is missing, is such mode transition a simple process (i.e. without mode swapping), or is it still a gradual progress with intermittent swapping?

In the present work, the primary goal is to explore the possible transition from pure mode A to mode B without any interference of vortex dislocations based on DNS. Therefore, only one spanwise wavelength of four diameters is taken into account, which is near the most unstable wavelength (Williamson 1996a, Henderson 1997). In the first part of the study (Lin 2023), a preliminary conclusion is given: in the absence of vortex dislocations, a mode swapping of pure modes A and B in the near wake still occurs when Re varies between 230 and 240. Thus, the spatiotemporal evolution of vorticity in the whole transition at Re $\in [190, 330]$ is analyzed in the second part of this study. In addition, because the spanwise phase is dependent on the specific spanwise position associated with vortices in pure modes A and B appearing on the rear surface and in the near wake, based on 3D stability analysis (Barkley and Henderson 1996, Posdziech and Grundmann 2001), we mainly focus on the varying spanwise positions of both modes A and B. The remainder of this paper is organized as follows. The governing equations coupled boundary conditions and numerical methods are first presented. Then, features in the vorticity signs in modes A and B and the spanwise phase transition between them are mainly investigated and discussed in detail. Finally, conclusions are presented.

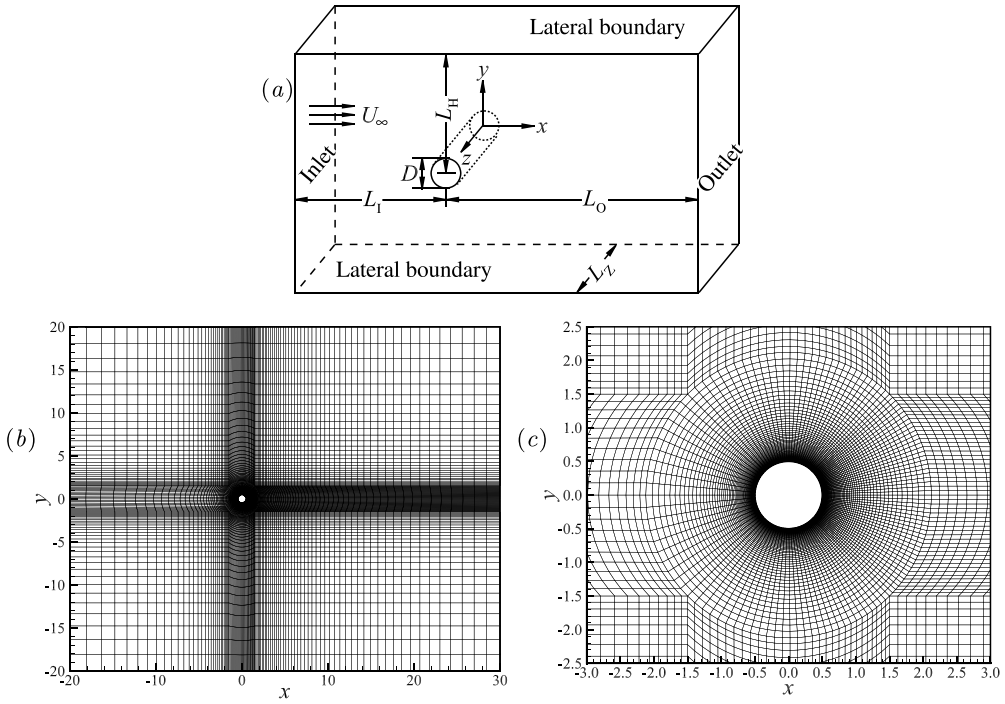

Figure 1. (a) Schematics of a flow past a straight cylinder with a circular cross-section, and computational domain in the (x, y) plane and mesh distributions in (b) the whole flow region and (c) near the cylinder with a closer view.

2. Numerical simulations

As shown in figure 1(a), the fluid flow past a fixed cylinder with a circular cross-section is studied. The fluid is incompressible with constant density ρ and kinematic viscosity ν. All body forces are conservative and can be reduced to components of pressure.

The inertial Cartesian coordinate system, (x, y, z), is established as shown in figure 1(a). Among the axes, the x-axis (streamwise direction) is aligned to the incoming free stream with uniform velocity U_∞. The z-axis (spanwise direction) is parallel to the cylinder span. The y-axis (vertical direction) is transverse to both the free stream and the cylinder axis.

The incompressible continuity and Navier–Stokes equations in dimensionless forms are written as:

$$\nabla \cdot \boldsymbol{u} = 0, \tag{2.1}$$

$$\frac{\partial \boldsymbol{u}}{\partial t} + (\boldsymbol{u} \cdot \nabla)\boldsymbol{u} = -\nabla p + \frac{1}{\mathrm{Re}}\nabla^2 \boldsymbol{u}, \tag{2.2}$$

where ∇ is the gradient operator, $\boldsymbol{u}$ is the velocity vector with three components (u, v, w) along their own coordinates, t is the time scaled by D/U_∞, p is the pressure scaled by ρU_∞^2, and Re is the Reynolds number defined by $U_\infty D/\nu$. The velocities are scaled by the free-steam velocity U_∞ and the lengths by the cylinder diameter D. Thus, all variables used in the following context are scaled by ρ, U_∞ and D.

Here, we describe the main variables and parameters involved in this study. The vorticity $\boldsymbol{\omega}$ is defined as the curl of velocity $\boldsymbol{u}$, i.e. $\boldsymbol{\omega} = \nabla \times \boldsymbol{u}$, with three components $(\omega_x, \omega_y, \omega_z)$ along their coordinates. As an important indicator in the present fluid dynamics, variations in the drag and lift forces acting on the body are taken into account and normalized as the drag and lift coefficients, C_{D} and C_{L}, respectively. Then, the mean drag coefficient, $\overline{C}_{\mathrm{D}}$, and the root-mean-square (RMS) lift coefficient, C'_{L}, are used to determine the intensity of fluid forces. When spanwise vortices are alternately shed in the near wake, the frequency of such a shedding vortex, f, is obtained through Fourier analysis of the time history of C_{L}. This value is scaled as the Strouhal number, St, which is defined by $St = fD/U_\infty$.

For the initial condition, the flow is assumed to be motionless with $\boldsymbol{u} = 0$ and $p = 0$ at $t = 0$, except at the inlet.

For the boundary conditions, as shown in figure 1(a), the 3D flow is first assumed to be spatially periodic across the span. At the inlet, the uniform free stream is prescribed as $u = U_\infty$ and $v = w = 0$. At the outlet, the simple outflow with $\partial \boldsymbol{u}/\partial x = 0$ is applied. At both lateral boundaries along the y-axis, the free-slip boundary condition with $\frac{\partial u}{\partial y} = v = \frac{\partial w}{\partial y} = 0$ is adopted. On cylinder surfaces, the no-slip boundary condition with $\boldsymbol{u} = 0$ is used. The reference pressure of $p_\infty = 0$ is specified at the center of the inlet.

As shown in figure 1(a), the entire nondimensional computational domain for the present wake flow is mainly captured through the inlet length $L_{\mathrm{I}} = 20$, the outlet length $L_{\mathrm{O}} = 30$, the vertical height $L_{\mathrm{H}} = 20$ and the computational spanwise length or cylinder span $L_{\mathrm{Z}} = 4$. Therefore, the 3D computational domain of present simulations, $(L_{\mathrm{I}} + L_{\mathrm{O}}) \times (L_{\mathrm{H}} + L_{\mathrm{H}}) \times L_{\mathrm{Z}}$, is $(20 + 30) \times (20 + 20) \times 4$. The blockage ratio β, as defined by $1/(2L_{\mathrm{H}})$, is thus equal to 2.5%.

The mesh distribution in the 2D computational domain is presented in figure 1(b). The smallest grid size of 0.001 is the normal distance of the first layer of the mesh next to the cylinder surface. A local mesh is mainly refined in the large circular region with a radial diameter of approximately 4.24, as shown in figure 1(c). A coarse mesh is mainly used far from the cylinder. The total element number of the present 2D mesh N_{xy} is 20 100. As already analyzed and reported in previous works (Henderson 1997, Lin and Tan 2019), a uniform spanwise grid size, $\Delta z = 0.1$, is estimated and adopted.

The dimensionless time step Δt is 0.01. Here, the maximal cell Courant number, $\mathrm{Co} = |u|\Delta t/\Delta l$, is less than approximately 0.8, where Δl is the cell size in the direction of the local velocity u through a cell.

Numerical calculations are performed using FLUENT V6.3.26 software with the finite-volume method. The viscous model adopts the 'Laminar' configuration. The pressure-implicit splitting of operators algorithm is applied as a pressure-velocity coupling scheme. For the discretization scheme, the second order is applied for the pressure equation; the second-order upwind scheme is used in solving the momentum equation; and the second-order implicit scheme is adopted in all unsteady formulations. In particular, the gradient computation is solved by the Green-Gauss node-based method.

The dimensionless error of the mass conservative equation (2.1), reaches the maximal error of $O(10^{-7})$, while the nondimensional errors of the three components of the momentum equation (2.2), are lower, on the order of $O(10^{-9})$.

The numerical model used here and independence studies about the computational domain and mesh distribution have already been validated in detail. For more details, we point interested readers to previous studies (Lin and Tan 2019, 2022, Lin 2022, 2023) that used the identical computational domain and mesh distributions.

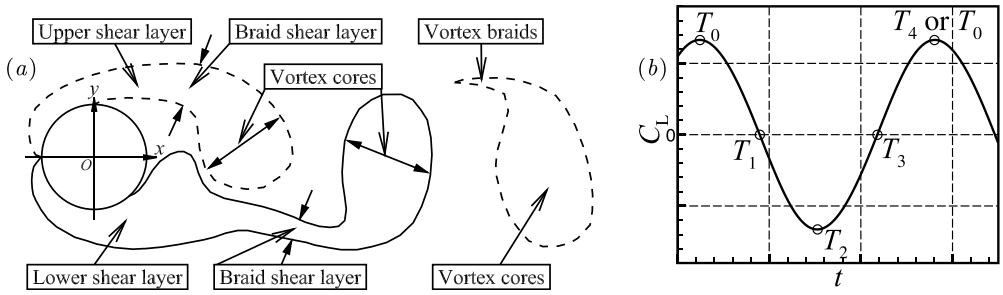

Figure 2. Schematic diagrams of (a) $+|\omega_z|$ and $-|\omega_z|$ denoted by solid and dashed lines, respectively, indicating the upper and lower shear layers, braid shear layers (Leweke and Williamson 1998), (shedding) vortex cores and braids in the near wake of a circular cylinder, and (b) four typical moments in a whole cycle of the fluctuating lift coefficient. Note that the position $y = 0$ on the rear surface denotes the vertical center on the rear surface, while the position $y = 0$ in the near wake denotes the wake center plane.

3. Results and discussion

In analyzing the characteristics of vorticity and its sign in pure modes A and B, we initially focus on the near wake (particularly the shear layers and the shedding primary vortices, which include the vortex braids and cores), as shown in figure 2(a). Then, we focus on the rear surface of the cylinder, and finally we focus on the relationship between the rear surface and the shear layers. Only vorticities with intensities greater than 10^{-3} in these regions are modeled and discussed. The results are analyzed and displayed primarily at specific moments, i.e. T_0 (or T_4), T_1, T_2 and T_3, as shown in figure 2(b).

In addition, for the sake of convenience, the sign of the nonzero vorticity ω is defined here by a sign function $\mathrm{sgn}(\omega)$ as

$$\mathrm{sgn}\,(\omega) = \begin{cases} +1, & \text{if } \omega > 0, \\ -1, & \text{if } \omega < 0. \end{cases} \tag{3.1}$$

3.1. Basic sign characteristics of additional vorticities in pure mode A

In the spatiotemporal evolution of pure mode A with the spanwise wavelength $\lambda_A = 4$ in the Re range from 100 to 200, there are two stages. When $140 < \mathrm{Re} < 193$, the first stage is the initial generation of pure mode A (Lin 2022), as shown in figure 3. When Re exceeds 193, pure mode A is in the full development stage (Lin and Tan 2019), as shown in figure 4. Regardless of these two stages in pure mode A, at the same spanwise position, there are special sign relationships of dominant additional vorticities, $(\omega_x)_A$ and $(\omega_y)_A$ (or ω_A), in the near wake summarized as follows:

$$\mathrm{sgn}\,(\omega_x)_{AN}\,(y > 0) = -\,\mathrm{sgn}\,(\omega_x)_{AN}\,(y < 0)\,, \tag{3.2a}$$

$$\mathrm{sgn}\,(\omega_y)_{AN}\,(y > 0) = +\,\mathrm{sgn}\,(\omega_y)_{AN}\,(y < 0)\,, \tag{3.2b}$$

$$\mathrm{sgn}\,(\omega_x)_{AN}\,(y > 0) = +\,\mathrm{sgn}\,(\omega_y)_{AN}\,(y > 0)\,, \tag{3.2c}$$

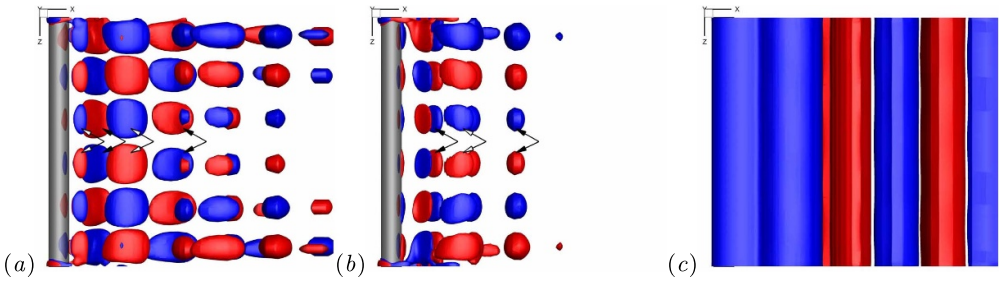

Figure 3. At $t = T_0$, top views of isosurfaces of (a) $\omega_x = \pm 0.01$, (b) $\omega_y = \pm 0.01$ and (c) $\omega_z = \pm 0.2$, in which the dominant vorticity is used in describing pure mode A at the initially generated stage in the near wake at Re $= 190$ (< 193) with $L_Z = 12$ (Lin 2022), where red and blue colors denote positive and negative values, respectively, and arrows with hollow and filled arrowheads denote vorticity originally generated or shed from the upper and lower shear layers, respectively. Note that the cylinder is denoted by the grey translucent surface and the flow is from left to right.

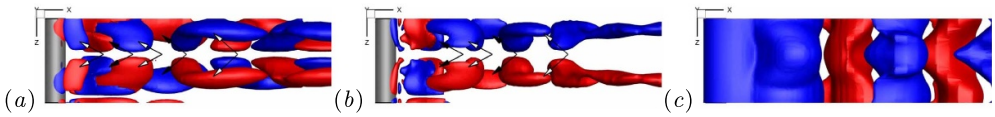

Figure 4. At $t = T_0$, top views of isosurfaces of (a) $\omega_x = \pm 0.2$, (b) $\omega_y = \pm 0.2$ and (c) $\omega_z = \pm 0.2$, in which the dominant vorticity is used in describing pure mode A at the fully developed stage in the near wake at Re $= 195$ ($\geqslant 193$) with $L_Z = 4$ (Lin and Tan 2019) (same descriptions as in figure 3).

$$\operatorname{sgn}(\omega_x)_{\mathrm{AN}}(y<0) = -\operatorname{sgn}(\omega_y)_{\mathrm{AN}}(y<0), \tag{3.2d}$$

where the subscript notations 'A' and 'N' indicate pure mode A and the near wake, respectively, and $y>0$ and $y<0$ indicate ω_{A} originally generated or shed from the upper and lower shear layers, respectively.

Next, as reported in previous works, additional vorticities in the near wake are generated on the rear surface (Lin and Tan 2019, Lin 2022). These also have special distributions in vorticity signs, as shown in figures 5 and 6 for the two stages. Typically, at $t = T_3$ and Re $= 190$, common characteristics for ω_{A} with λ_{A} at the same spanwise position are summarized as follows:

$$\operatorname{sgn}(\omega_x)_{\mathrm{AR}}(y>0) = +\operatorname{sgn}(\omega_x)_{\mathrm{AR}}(y<0), \tag{3.3a}$$

$$\operatorname{sgn}(\omega_y)_{\mathrm{AR}}(y>0) = -\operatorname{sgn}(\omega_y)_{\mathrm{AR}}(y<0), \tag{3.3b}$$

$$\operatorname{sgn}(\omega_x)_{\mathrm{AR}}(y>0) = -\operatorname{sgn}(\omega_y)_{\mathrm{AR}}(y>0), \tag{3.3c}$$

$$\operatorname{sgn}(\omega_x)_{\mathrm{AR}}(y<0) = +\operatorname{sgn}(\omega_y)_{\mathrm{AR}}(y<0), \tag{3.3d}$$

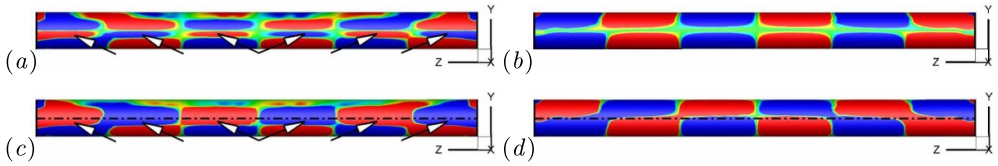

Figure 5. At Re = 190 with $L_Z = 12$, on the rear surface, contours of ω_x at (a) $t = T_0$ and (b) T_3, and ω_y at (c) $t = T_0$ and (d) T_3, in which the dominant vorticity is used in describing pure mode A at the initial generation stage (Lin 2022), where red and blue colors denote positive and negative values, respectively, green color indicates vorticity almost zero, i.e. $|\omega| < 10^{-3}$, dotted dash lines denote the center position $y = 0$, and arrows at $t = T_0$ denote the disturbed vorticity with a spanwise wavelength λ_A but its vorticity sign is different from that in pure mode A, e.g. subfigures (b) and (d) at $t = T_3$.

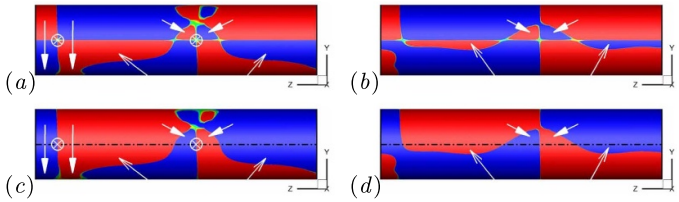

Figure 6. At Re = 195 with $L_Z = 4$, on the rear surface, contours of ω_x at (a) $t = T_0$ and (b) T_3, and ω_y at (c) $t = T_0$ and (d) T_3, in which the dominant vorticity is used in describing pure mode A at the full development stage (Lin and Tan 2019), where arrows with plain arrowheads denote the disturbed vorticity, the same as in figure 5, near $y = 0$ with $\lambda_A = 4$, and arrows with filled arrowheads denote the disturbed vorticity with smaller spanwise wavelengths $\frac{1}{6}L_Z$ and $\frac{1}{4}L_Z$ at T_0 and T_3, respectively. Symbols $\otimes$ at $y = 0$ denote the 'end' positions, $z = 1.71$ and 3.7, at which $\omega_x = \omega_y = 0$.

where the subscript 'R' denotes the rear surface, and $y > 0$ and $y < 0$ on the rear surface indicate ω_A at the upper and lower sides of the vertical center $y = 0$ on the rear surface, respectively. Moreover, as shown by arrows in figures 5 and 6, there is the disturbed vorticity on the rear surface, as well as in the near wake, as respectively denoted by '$(\omega_x)_{DA}$' and '$(\omega_y)_{DA}$' (or 'ω_{DA}'). This disturbed or perturbed vorticity exhibits a spanwise wavelength λ_{DA} and/or vorticity sign that is different from that expressed by equations (3.2) and (3.3) in pure mode A.

Finally, at $t = T_0$, as shown in figures 3 and 5 at Re = 190 or figures 4 and 6 at Re = 195, the sign relationship between ω_A in the near wake and on the rear surface can be expressed at the same spanwise position as follows:

$$\operatorname{sgn}(\omega_x)_{AN}(T_0, y > 0) = -\operatorname{sgn}(\omega_x)_{AR}(T_0, y > 0), \tag{3.4a}$$

$$\operatorname{sgn}(\omega_x)_{AN}(T_0, y < 0) = +\operatorname{sgn}(\omega_x)_{AR}(T_0, y < 0), \tag{3.4b}$$

$$\operatorname{sgn}(\omega_y)_{AN}(T_0, y > 0) = +\operatorname{sgn}(\omega_y)_{AR}(T_0, y > 0), \tag{3.4c}$$

$$\operatorname{sgn}(\omega_y)_{AN}(T_0, y < 0) = -\operatorname{sgn}(\omega_y)_{AR}(T_0, y < 0). \tag{3.4d}$$

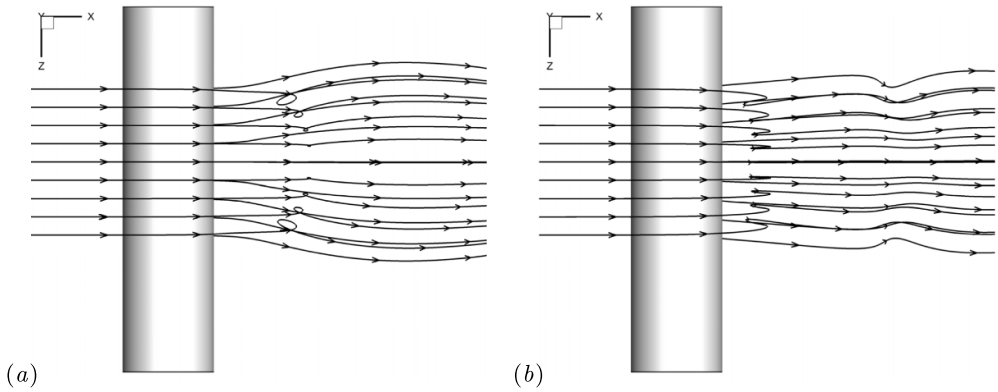

Figure 7. At Re = 195 with $L_Z = 4$ in pure mode A, top views of typical streamlines past the cylinder at (a) $t = T_0$ and (b) T_3 near $z = 1.71$, where the grey surface denotes the cylinder.

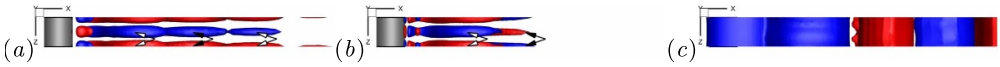

Figure 8. At $t = T_0$, top views of isosurfaces of (a) $\omega_x = \pm 0.2$, (b) $\omega_y = \pm 0.1$ and (c) $\omega_z = \pm 0.2$, in which the dominant vorticity is used in illustrating pure mode B in the near wake at Re = 300 with $L_Z = 1$ (Lin and Tan 2022) (same descriptions as in figure 3).

In addition, as shown in figure 7 at Re = 195, near the special position $z = 1.71$ at two typical times T_0 and T_3, adjacent streamlines bypassing the upper surface (in the upper shear layer) are close to each other at $x < 1$, while adjacent streamlines that bypass the lower surface (in the lower shear layer) are far from each other. This phenomenon, i.e. the parallel streamlines near the cylinder surface varying wavily across the span, is well consistent with that reported by Yokoi and Kamemoto (1992, 1993).

3.2. Basic sign characteristics of additional vorticities in pure mode B

Pure mode B is mainly presented in 3D computations with $L_Z = 1$, as shown in figure 8, and further confirmed in simulations with $L_Z = 2$ and 4 (such as figures 11–14 at typical Reynolds numbers of 310 and 320 in the section 3.4). The typical spanwise wavelength λ_B is 1. According to previous work (Lin and Tan 2022), the characteristics of additional vorticity signs in pure mode B, $(\omega_x)_B$ and $(\omega_y)_B$ (or ω_B), at the same spanwise position are obtained in the near wake as follows:

$$\operatorname{sgn}(\omega_x)_{BN}(y > 0) = +\operatorname{sgn}(\omega_x)_{BN}(y < 0), \tag{3.5a}$$

$$\operatorname{sgn}(\omega_y)_{BN}(y > 0) = -\operatorname{sgn}(\omega_y)_{BN}(y < 0), \tag{3.5b}$$

$$\operatorname{sgn}(\omega_x)_{BN}(y > 0) = +\operatorname{sgn}(\omega_y)_{BN}(y > 0), \tag{3.5c}$$

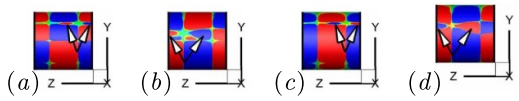

Figure 9. At Re = 300 with $L_Z = 1$, on the rear surface, contours of ω_x at (a) $t = T_0$ and (b) T_1, and ω_y at (c) $t = T_0$ and (d) T_1, in which the dominant vorticity is used in describing pure mode B (Lin and Tan 2022), where red and blue colors denote positive and negative values, respectively, and green color denotes vorticity almost zero, i.e. $|\omega| < 10^{-3}$. Note that the disturbed vorticity, denoted by arrows, has a spanwise wavelength λ_B but its vorticity sign is different from that in pure mode B.

$$\operatorname{sgn}(\omega_x)_{BN}(y<0) = -\operatorname{sgn}(\omega_y)_{BN}(y<0), \tag{3.5d}$$

where the subscript 'B' denotes pure mode B.

Next, as shown in figure 9, neglecting the effect of disturbed vorticity denoted by arrows on the main distribution of ω_B on the rear surface, common features of ω_B signs at the same spanwise position can be expressed as follows:

$$\operatorname{sgn}(\omega_x)_{BR}(y>0) = -\operatorname{sgn}(\omega_x)_{BR}(y<0), \tag{3.6a}$$

$$\operatorname{sgn}(\omega_y)_{BR}(y>0) = +\operatorname{sgn}(\omega_y)_{BR}(y<0), \tag{3.6b}$$

$$\operatorname{sgn}(\omega_x)_{BR}(y>0) = -\operatorname{sgn}(\omega_y)_{BR}(y>0), \tag{3.6c}$$

$$\operatorname{sgn}(\omega_x)_{BR}(y<0) = +\operatorname{sgn}(\omega_y)_{BR}(y<0). \tag{3.6d}$$

Similarly, as shown by arrows in figure 9, there is also the disturbed vorticity on the rear surface, as well as in the near wake, denoted by '$(\omega_x)_{DB}$' and '$(\omega_y)_{DB}$' (or 'ω_{DB}'). This disturbed vorticity has a spanwise wavelength and/or vorticity sign different from that expressed by equations (3.6) and (3.5) in pure mode B.

As a result, at $t = T_0$, as shown in figures 8 and 9 at Re = 300, the sign relationship between dominant additional vorticities in the near wake and on the rear surface can be expressed at the same spanwise position as follows:

$$\operatorname{sgn}(\omega_x)_{BN}(T_0, y>0) = +\operatorname{sgn}(\omega_x)_{BR}(T_0, y>0), \tag{3.7a}$$

$$\operatorname{sgn}(\omega_x)_{BN}(T_0, y<0) = -\operatorname{sgn}(\omega_x)_{BR}(T_0, y<0), \tag{3.7b}$$

$$\operatorname{sgn}(\omega_y)_{BN}(T_0, y>0) = -\operatorname{sgn}(\omega_y)_{BR}(T_0, y>0), \tag{3.7c}$$

$$\operatorname{sgn}(\omega_y)_{BN}(T_0, y<0) = +\operatorname{sgn}(\omega_y)_{BR}(T_0, y<0). \tag{3.7d}$$

Moreover, as shown in figure 10, regardless of whether $L_Z = 4$ or 1 in pure mode B, adjacent streamlines bypassing both sides of the cylinder at $x < 1$ are almost parallel to each other or slightly skewed across the span.

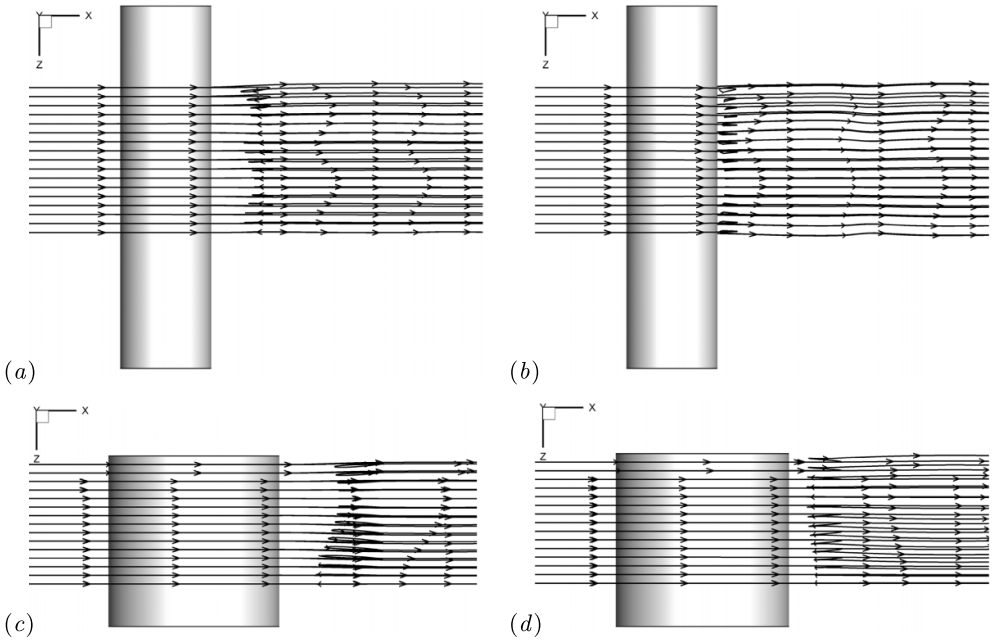

Figure 10. In pure mode B, top views of typical streamlines past the cylinder at (a) $t = T_0$ and (b) T_3 when $\mathrm{Re} = 270$ and $L_Z = 4$, and at (c) $t = T_0$ and (d) T_1 when $\mathrm{Re} = 300$ and $L_Z = 1$. Note that the cylinder is denoted by the grey surface.

In summary, these special sign characteristics of additional vorticities on the rear surface and in the near wake are helpful in identifying pure mode A or B in the following spanwise phase transition.

3.3. Relationship between pure modes A and B

3.3.1. Vorticity sign relationships. Based on the above sign features in pure modes A and B at the same spanwise position, there are two common sign relationships. The first in the near wake, already presented in previous studies (Lin *et al* 2018a, Lin and Tan 2019, 2022), is summarized as follows:

$$\mathrm{sgn}\,(\omega_x)_{\mathrm{N}}\,(y>0) = +\,\mathrm{sgn}\,(\omega_y)_{\mathrm{N}}\,(y>0)\,, \tag{3.8a}$$

$$\mathrm{sgn}\,(\omega_x)_{\mathrm{N}}\,(y<0) = -\,\mathrm{sgn}\,(\omega_y)_{\mathrm{N}}\,(y<0)\,. \tag{3.8b}$$

However, the second on the rear surface is obtained as follows:

$$\mathrm{sgn}\,(\omega_x)_{\mathrm{R}}\,(y>0) = -\,\mathrm{sgn}\,(\omega_y)_{\mathrm{R}}\,(y>0)\,, \tag{3.9a}$$

$$\mathrm{sgn}\,(\omega_x)_{\mathrm{R}}\,(y<0) = +\,\mathrm{sgn}\,(\omega_y)_{\mathrm{R}}\,(y<0)\,. \tag{3.9b}$$

Accordingly, the sign relationship of the first sign variable between additional vorticities, defined by $\varpi_1 = \omega_x \cdot \omega_y$, originally (generated and/or shedding) from the upper and lower shear layers at the same spanwise position is presented as follows:

$$\mathrm{sgn}\,(\varpi_1)_{\mathrm{N}}\,(y > 0) = +1, \tag{3.10a}$$

$$\mathrm{sgn}\,(\varpi_1)_{\mathrm{N}}\,(y < 0) = -1, \tag{3.10b}$$

$$\mathrm{sgn}\,(\varpi_1)_{\mathrm{N}}\,(y > 0) = -\,\mathrm{sgn}\,(\varpi_1)_{\mathrm{N}}\,(y < 0)\,. \tag{3.10c}$$

This corresponds to the first vorticity sign law in both pure modes A and B (Lin *et al* 2018a, 2018b, 2019a, Lin and Tan 2019, 2022).

Moreover, while the spanwise vorticity in the near wake is taken into account, such as ω_z in the vortex cores in figure 2(a), the vorticity sign relationship of the spanwise vorticity originally (generated and/or shedding) from the upper and lower shear layers at the same spanwise position is also summarized as follows:

$$\mathrm{sgn}\,(\omega_z)_{\mathrm{N}}\,(y > 0) = -1, \tag{3.11a}$$

$$\mathrm{sgn}\,(\omega_z)_{\mathrm{N}}\,(y < 0) = +1, \tag{3.11b}$$

$$\mathrm{sgn}\,(\omega_z)_{\mathrm{N}}\,(y > 0) = -\,\mathrm{sgn}\,(\omega_z)_{\mathrm{N}}\,(y < 0)\,. \tag{3.11c}$$

Consequently, the sign relationship of the second sign variable among vorticities, defined by $\varpi_2 = \omega_x \cdot \omega_y \cdot \omega_z$, originally (generated and/or shedding) from the upper and lower shear layers at the same spanwise position is presented as follows:

$$\mathrm{sgn}\,(\varpi_2)_{\mathrm{N}} = -1. \tag{3.12}$$

This corresponds to the second vorticity sign law in both pure modes A and B (Lin *et al* 2018a, 2018b, 2019a, Lin and Tan 2019, 2022).

Generally, the vorticity on the rear surface, which is often overlooked in previous studies, in fact contributes greatly to the spatiotemporal evolution of the vorticity in the near wake of both pure modes A and B. When additional vorticities are generated on the rear surface due to 3D instability, such vorticity on the rear surface enters the shear layers either through the convective transport mechanism of inertial forces or through the vortex-induced vortex mechanism of viscous forces, as has been reported previously (Yokoi and Kamemoto 1992, 1993, Lin and Tan 2019, 2022, Lin *et al* 2019a, 2019b, Lin 2022). These different physical mechanisms correspond to different generation mechanisms of the streamwise or vertical vorticity in pure mode A or B. Therefore, in the following analysis, we focus mainly on the characteristics of vorticities and their signs on the rear surface and in the near wake, which are associated with pure modes A and B, and in particular, the physical relationship between disturbed vorticity (ω_{DA}) and additional vorticities in pure mode B (ω_{B}) at $\mathrm{Re} \geqslant 193$.

3.3.2. Spatiotemporal symmetry. A type of spatiotemporal symmetry of pure mode A was observed through the 3D Floquet stability analysis (Barkley and Henderson 1996, Robichaux *et al* 1999) of the wakes of circular and square cylinders as follows,

$$(\omega_x)_{\mathrm{AN}}(t,x,y,z) = -(\omega_x)_{\mathrm{AN}}(t+T/2,x,-y,z), \tag{3.13a}$$

$$(\omega_y)_{\mathrm{AN}}(t,x,y,z) = +(\omega_y)_{\mathrm{AN}}(t+T/2,x,-y,z) \tag{3.13b}$$

where T is the time period of vortex shedding and $y=0$ is the wake center plane. This phenomenon is also referred to as reflection-translation (RT) symmetry. Similarly, for pure mode B, the RT symmetry is expressed by

$$(\omega_x)_{\mathrm{BN}}(t,x,y,z) = +(\omega_x)_{\mathrm{BN}}(t+T/2,x,-y,z), \tag{3.14a}$$

$$(\omega_y)_{\mathrm{BN}}(t,x,y,z) = -(\omega_y)_{\mathrm{BN}}(t+T/2,x,-y,z). \tag{3.14b}$$

Accordingly, for both pure modes A and B, a basic relationship for the combination of ω_x and ω_y at a specific space and time can be written as

$$(\varpi_1)_{\mathrm{N}}(t,x,y,z) = -(\varpi_1)_{\mathrm{N}}(t+T/2,x,-y,z). \tag{3.15}$$

Several characteristics of this RT symmetry are summarized as follows:

(1) The sign of ϖ_1 at $y>0$ is always opposite to that at $y<0$ after a half T-period translation, i.e. the odd RT symmetry for ϖ_1, expressed by:
$$\mathrm{sgn}(\varpi_1)_{\mathrm{N}}(t,y) = -\mathrm{sgn}(\varpi_1)_{\mathrm{N}}(t+T/2,-y). \tag{3.16}$$
(2) There exist two possible sign combinations on the upper side of the wake center plane, as an example. For example, one can be $\mathrm{sgn}(\varpi_1)(y)=+1$ and the other can be $\mathrm{sgn}(\varpi_1)(y)=-1$. The first sign relationship is consistent with the first sign law, equation (3.10). However, the second breaks the sign laws and is also not reported elsewhere for either pure mode A or B. Therefore, the RT symmetry cannot reveal the intrinsic physical relationship between ω_x and ω_y in the same space and time.
(3) The intrinsic relationship of ω_x or ω_y between the upper and lower sides of the wake center plane illustrated in equation (3.13) or (3.14), respectively, is T periodic. In particular, in the present pure mode A, the streamwise vorticity obeys an odd RT symmetry, while the vertical vorticity obeys an even RT symmetry. For pure mode B, these symmetries in ω_x and ω_y are opposite to those in pure mode A. This feature clearly demonstrates that there is no intrinsic physical relationship between the vorticity fields of pure modes A and B.
(4) However, the odd RT symmetry for ϖ_1 further indicates that a certain feature exists that is a type of vorticity relationship between pure modes A and B.

Furthermore, if the RT symmetry of ω_z is taken into account, it is expressed by

$$(\omega_z)_{\mathrm{N}}(t,x,y,z) = -(\omega_z)_{\mathrm{N}}(t+T/2,x,-y,z). \tag{3.17}$$

The extended combination of the three vorticity components based on equations (3.15) and (3.17) is obtained as

$$(\varpi_2)_{\mathrm{N}}(t,x,y,z) = +(\varpi_2)_{\mathrm{N}}(t+T/2,x,-y,z). \tag{3.18}$$

Similarly, some characteristics are presented as follows:

(1) The sign of ϖ_2 at $y>0$ is always the same as that at $y<0$ after a half T-period translation, i.e. the even RT symmetry for ϖ_2, expressed by:

$$\mathrm{sgn}\,(\varpi_2)_{\mathrm{N}}\,(t,y) = +\mathrm{sgn}\,(\varpi_2)_{\mathrm{N}}\,(t+T/2,-y)\,. \tag{3.19}$$

(2) There remain two possible sign combinations in the near wake, regardless of the upper or lower side of the wake center plane. One is $\mathrm{sgn}(\varpi_2)=+1$, while the other is $\mathrm{sgn}(\varpi_2)=-1$. The second sign relationship is clearly consistent with the second sign law, equation (3.12). However, the first breaks the second sign law, regardless of pure mode A or B. This observation further confirms that the RT symmetry cannot reveal the intrinsic physical relationship among ω_x, ω_y and ω_z at the same space and time.
(3) The even RT symmetry for ϖ_2 is also T periodic, which clearly shows that a type of intrinsic physical relationship between the vorticity fields of (pure) modes A and B truly exists.

For the present two vorticity sign laws in the near wake, different characteristics are presented:

(1) The first sign law, equation (3.10), clearly shows an intrinsic physical relationship between ω_x and ω_y in both pure modes A and B.
(2) The second sign law, equation (3.12), also demonstrates an intrinsic relationship among the three components of vorticity for both pure modes A and B.
(3) Intrinsic physical relationships between pure modes A and B are illustrated by the two sign laws of vorticity given in equations (3.10) and (3.12).
(4) These sign laws are independent of time in the present periodic flow, even in a steady wake flow of a bluff body under a certain geometric disturbance (Lin *et al* 2018b, Lin 2020).

In summary, the RT symmetry shows only the individual features for pure mode A or B under temporal evolution, while the vorticity sign law reveals the intrinsic features of different vorticity components and the common characteristics between pure modes A and B independent of time and periodic flow. Therefore, the vorticity sign laws are universal in describing pure modes A and B.

3.4. Evolution of additional vorticities in the spanwise phase transition

Based on a detailed comparison among the spatiotemporal evolution of the three vorticity components in the near wake and on the rear surface, as shown in figures 11–20, the complete transition from pure mode A to mode B in the Reynolds number range from 190 to 330 is basically divided into four stages. Among these stages, the first stage, i.e. the initial generation stage of pure mode A, does not show any sign of mode B when Re is below 193 (± 0.5) (Lin 2023). In the second stage, when Re is less than 230, pure mode A is fully developed, and the sign feature of additional vorticities in mode B appears partially in the shear layers and on the rear surface. Subsequently, the third stage at $\mathrm{Re}\in[230, 260\sim 265)$ indicates that modes A and B in the near wake coexist in the gradual transition or mode swapping. Finally, when Re exceeds 265, mode B is completely dominant in the near wake. This general transition process is consistent with the previous experiments and DNS with $L_Z=12$ (Williamson 1996a, Jiang *et al* 2016).

3.4.1. In the first stage at Re < 193. In this stage, the strength of additional vorticities is as low as approximately $O(10^{-2})$, as shown in figure 3. This result leads to only the spanwise

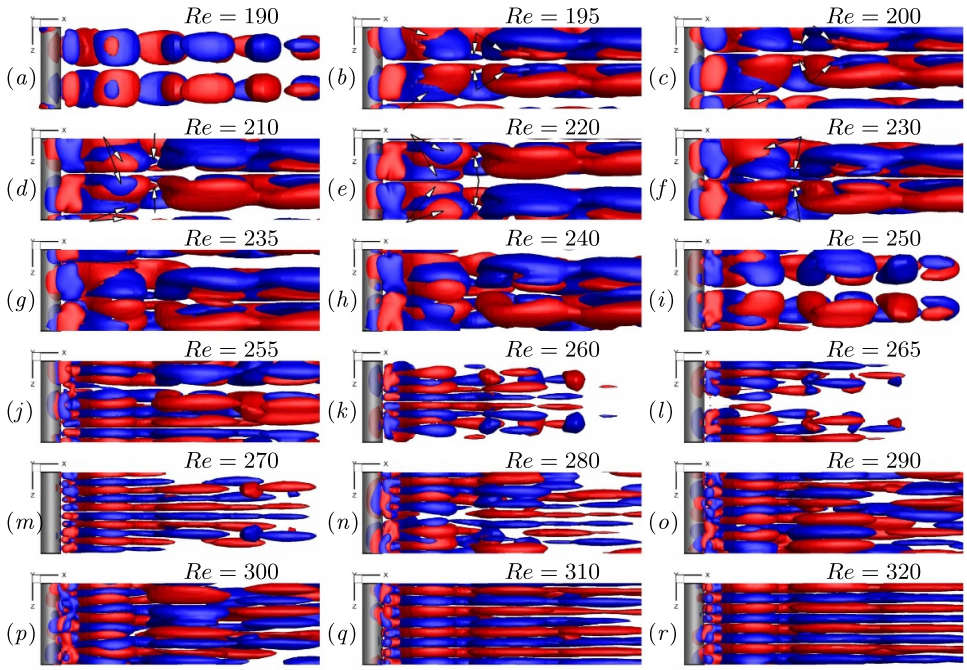

Figure 11. At $t = T_0$ with $L_Z = 4$, top views of isosurfaces of $\omega_x = \pm 0.02$ (Re $= 190$) and ± 0.1 (Re $\geqslant 195$) in the near wake at different Reynolds numbers, where red and blue colors denote positive and negative values, respectively, and arrows denote $(\omega_x)_{\mathrm{DA}}$. Note that the cylinder is denoted by the grey translucent surface and the flow is from left to right. Particularly, when Re $\in [230, 240]$, only results with fluid forces at a low level are presented here.

vortex braids being slightly wavily distorted across the span. However, the primary vortex cores are still 2D. This effect offers a physical explanation for why the hydrodynamic parameters, such as $\overline{C}_{\mathrm{D}}$, C'_{L} and St, agree well with those given by a 2D flow simulation (Lin 2022, 2023).

Moreover, the disturbed vorticity ω_{DA}, in which λ_{DA} is equal to λ_{A}, exhibits a different vorticity sign on the rear surface at a certain moment. Typically, as shown in figure 5, ω_{DA} almost disappears at $t = T_3$. However, $\pm|(\omega_x)_{\mathrm{DA}}|$ and $\pm|(\omega_y)_{\mathrm{DA}}|$, denoted by arrows, exist only in the region of $y < 0$ at $t = T_0$. The appearance of $\pm|\omega_{\mathrm{DA}}|$ at $t = T_0$ is actually caused by the expansion or growth of the clockwise spanwise vortex (with $-|\omega_z|$) near the upper and rear surface at $t = T_3$, as shown in figure 21. This expansion causes the vertical vortices (with $\pm|\omega_y|$) originally distributed on the upper and rear surface to extend downward across the central position $y = 0$, based on the fact that $\mathrm{sgn}(\omega_y)_{\mathrm{DA}}(y < 0)$ is exactly the same as $\mathrm{sgn}(\omega_y)_{\mathrm{A}}(y > 0)$. Meanwhile, $\pm|(\omega_x)_{\mathrm{DA}}|$ also satisfies the sign relationship with $\pm|(\omega_y)_{\mathrm{DA}}|$ on the lower and rear surface at the same spanwise position, i.e. equation (3.3*d*). These characteristics in the signs of ω_{DA} can help exclude features caused by pure mode A and clarify the appearance of pure mode B in the mode transition.

3.4.2. In the second stage at $193 \leqslant Re < 230$. We note the following labels used in the figures:

VorX0-U and VorX0-D: $(\omega_x)_{\mathrm{A}}$ (denoted by 'VorX') initially generated and/or increasing in the upper (denoted by 'U') and lower/down (denoted by 'D') shear layers, respectively.

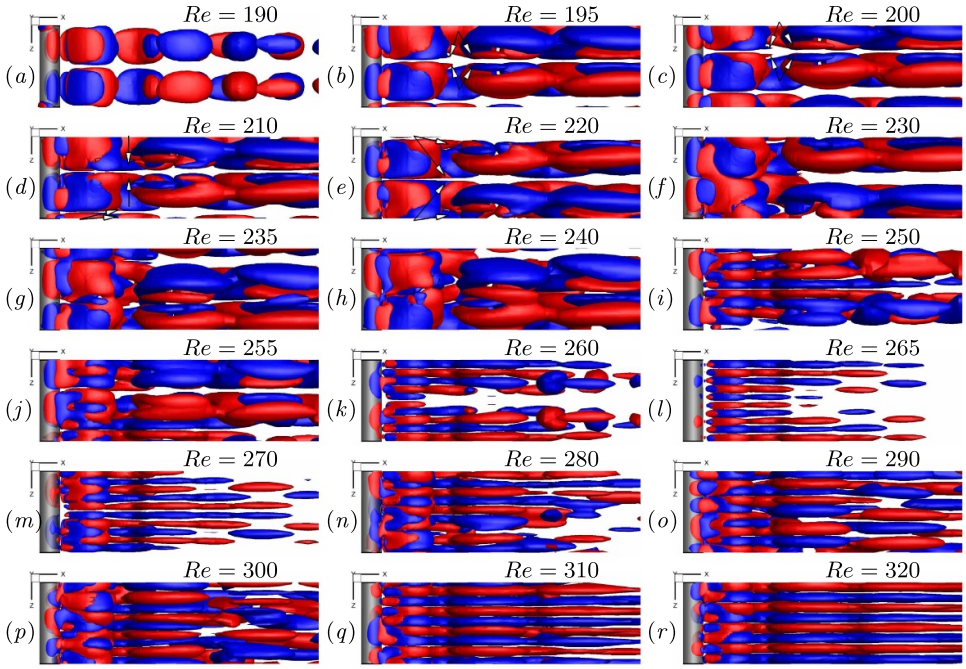

Figure 12. At $t = T_3$ with $L_Z = 4$, top views of isosurfaces of $\omega_x = \pm 0.02$ (Re $= 190$) and ± 0.1 (Re $\geqslant 195$) in the near wake at different Reynolds numbers (same descriptions as in figure 11).

VorX1-U and VorX1-D: $(\omega_x)_{\rm A}$ (denoted by 'VorX') concentrated and/or immediately shedding from the upper (denoted by 'U') and lower/down (denoted by 'D') shear layers, respectively.

Similar labels, VorY0-U, VorY0-D, VorY1-U and VorY1-D, are prescribed for $(\omega_y)_{\rm A}$ (denoted by 'VorY') in the figures.

In this stage, the strength of additional vorticities reaches $O(10^{-1})$, as shown in figure 4. This results in both the primary vortex braids and cores being significantly distorted along the spanwise direction. The near wake is 3D. As shown in figure 22, based on the different distortion effects of streamwise and vertical interactions (Meiburg and Lasheras 1988, Lin *et al* 2018b), the main twisting mechanism of spanwise vortices here can be attributed to the vertical interaction. Consequently, the hydrodynamic parameters all drop suddenly when Re exceeds 193 (Lin 2023).

For $\omega_{\rm DA}$, in addition to $\omega_{\rm DA}$ with $\lambda_{\rm A}$ mainly distributed near $y = 0$, similar to that at Re $<$ 193, there is $\omega_{\rm DA}$ with a smaller $\lambda_{\rm DA}$ (close to $\lambda_{\rm B}$) on the rear surface and in the shear layers. Typically, as shown by the filled arrows in figure 6 on the rear surface at Re $= 195$, $\omega_{\rm DA}$ appears near one side of $y = 0$ but at different spanwise positions, such as the position near $z = 1.71$ at both times T_0 and T_3 but the position near $z = 3.7$ only at T_0. $\lambda_{\rm DA}$ changes from $\frac{1}{4}L_Z$ at $t = T_3$ to $\frac{1}{6}L_Z$ at T_0.

In the shear layers or the near wake, typically as shown in figure 4 at Re $= 195$ (see also figures 11–14), there are three kinds of $\omega_{\rm DA}$ with $\lambda_{\rm DA}$ ($< \lambda_{\rm A}$):

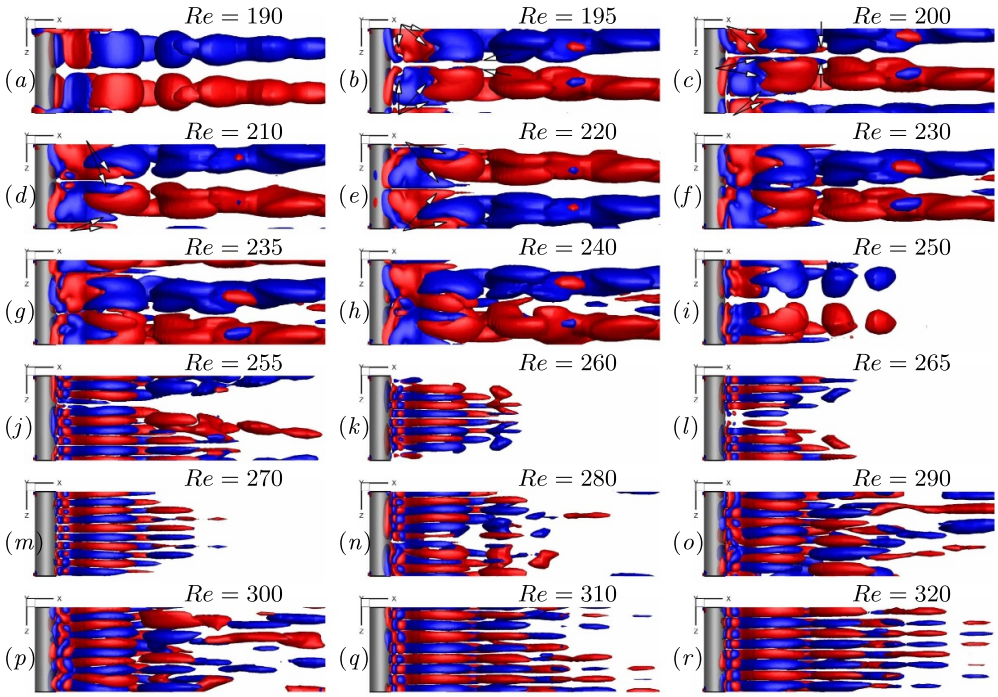

Figure 13. At $t = T_0$ with $L_Z = 4$, top views of isosurfaces of $\omega_y = \pm 0.01$ (Re $= 190$) and ± 0.1 (Re $\geqslant 195$) in the near wake at different Reynolds numbers, where red and blue colors denote positive and negative values, respectively, and arrows denote $(\omega_y)_{\mathrm{DA}}$. Note that the cylinder is denoted by the grey translucent surface and the flow is from left to right. Particularly, when Re $\in [230, 240]$, only results with fluid forces at a low level are presented here.

(1) The first type is mainly distributed in the (braid) shear layers just beside the cylinder near specific spanwise positions. Typically, as shown in figure 23, these spanwise positions, i.e. $z = 1.71$ and 3.7, are defined as the 'end' positions with a spacing of (approximately) $\frac{1}{2}\lambda_{\mathrm{A}}$, while other positions between these 'end' positions, e.g. $1.71 < z < 3.7$, are defined as the 'middle' positions. The sign of ω_{DA} is opposite to that of ω_{A}. By comparing the spanwise position of ω_{DA} on the rear surface and in the shear layers, as shown in figures 4, 6 and 23, ω_{DA} primarily appears near both 'end' positions. Meanwhile, λ_{DA1} (approximately $\frac{1}{6}L_Z$) in the lower shear layer at $t = T_3$ in figure 23 is actually correlated with that on the rear surface at $t = T_2$, similar to that in figure 6 at $t = T_0$. Notice that $(\omega_y)_{\mathrm{DA}}$ near both $z = 1.71$ and 3.7 and $(\omega_x)_{\mathrm{DA}}$ near $z = 3.7$ originate from those in the lower shear layer, while $(\omega_x)_{\mathrm{DA}}$ near $z = 1.71$ could be initially induced by the vortex-induced vortex mechanism (i.e. $\pm|\omega_x|$ induced by $\mp|\omega_y|$, respectively) by viscous forces or the convective transport and vortex-stretching mechanism by inertial forces (Lin and Tan 2019, 2022).

(2) The second type occurs within the range of λ_{DA2} from $\frac{1}{5}L_Z$ to $\frac{1}{3}L_Z$ at the 'middle' positions and causes spanwise waviness in the isosurfaces of additional vorticities in the near wake. Typically, as illustrated in figures 4 and 23, isosurfaces of $\pm|\omega_y|$ have wavy characteristics at the 'middle' region of $1.71 < z < 3.7$ in the (braid) shear layers and the near wake, which are different from those at Re $= 190$ in figure 3(b). The physical reason for this distinction is attributed to the superposition of vorticity with (at least) three different

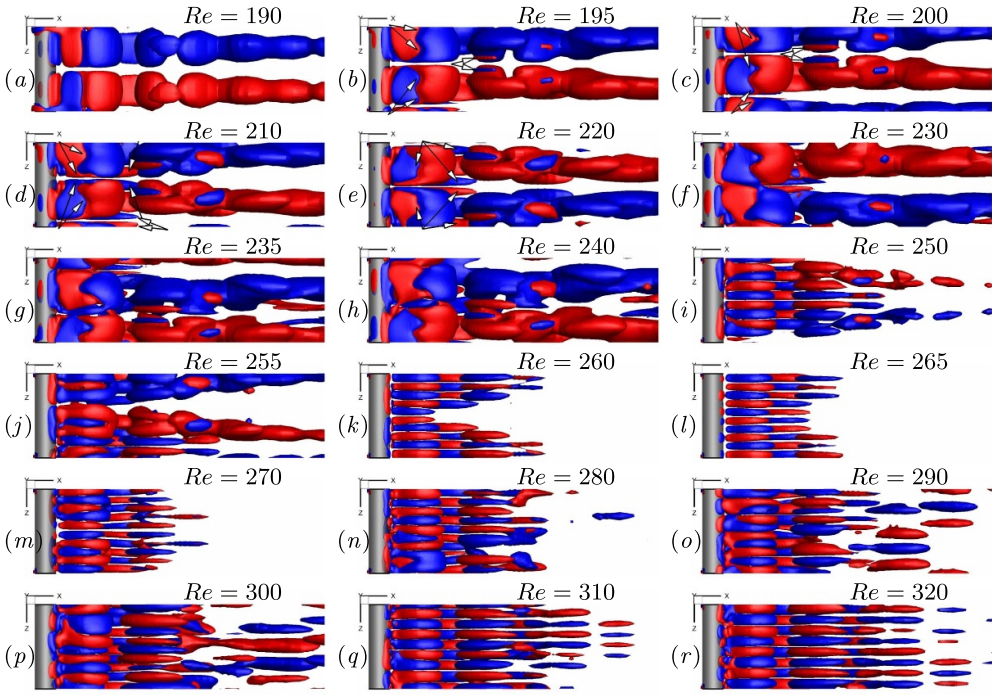

Figure 14. At $t = T_3$ with $L_Z = 4$, top views of isosurfaces of $\omega_y = \pm 0.01$ (Re $= 190$) and ± 0.1 (Re $\geqslant 195$) in the near wake at different Reynolds numbers (same descriptions as in figure 13).

wavelengths across the span, such as $L_Z = 4$, $\frac{1}{4}L_Z = 1$ and $\frac{1}{5}L_Z = 0.8$, as analyzed qualitatively in appendix A. This feature of the wavy isosurface in both shear layers indicates that the present kind of disturbed vorticity with a wavelength λ_{DA2} of 0.8 or 1 is already generated and exists across the span.

(3) The third type is mainly distributed in the first (immediately) shedding primary vortex with λ_{DA3} around $\frac{1}{4}L_Z$ near the 'end' positions. It typically appears as 'rib'-like contours of ω_x and ω_y in figures 24 and 25 at Re < 230. ω_{DA} is quickly weakened and disappears when the first primary vortex is further shedding far away from the body. The specific spanwise positions are consistent with those of ω_{DA} on the rear surface of the cylinder, such as $z = 1.46$ at $t = T_0$ and Re $= 195$, as shown in figures 6 and 24, and $z = 0.3$ at $t = T_3$ and Re $= 220$, as shown in figures 16(e) and 25, and are also consistent with those of the first kind of ω_{DA}, such as near $z = 1.71$ illustrated in figure 23. Therefore, the third kind actually originates from the first kind further shedding with the alternately shedding primary vortex, in which the increase in λ_{DA} from λ_{DA1} to λ_{DA3} is possibly caused by the viscous diffusion coupling the nonlinear vortex stretching effect.

Through the comparison of additional vorticities, we determined that the above ω_{DA} distributed on the rear surface and in the shear layers or the near wake conforms to some characteristics of pure mode B in the smaller spanwise wavelength and the vorticity sign relationship. For example, in the near wake, as shown in figures 24 and 25 at the same spanwise position, $\mathrm{sgn}(\omega_x)_{DA}$ is the same as that in the upper shear layer, while $\mathrm{sgn}(\omega_y)_{DA}$ is the opposite of that in the upper shear layer, which agrees well with equation (3.5). In summary, these results strongly support that pure mode B actually appears initially on the rear surface and the

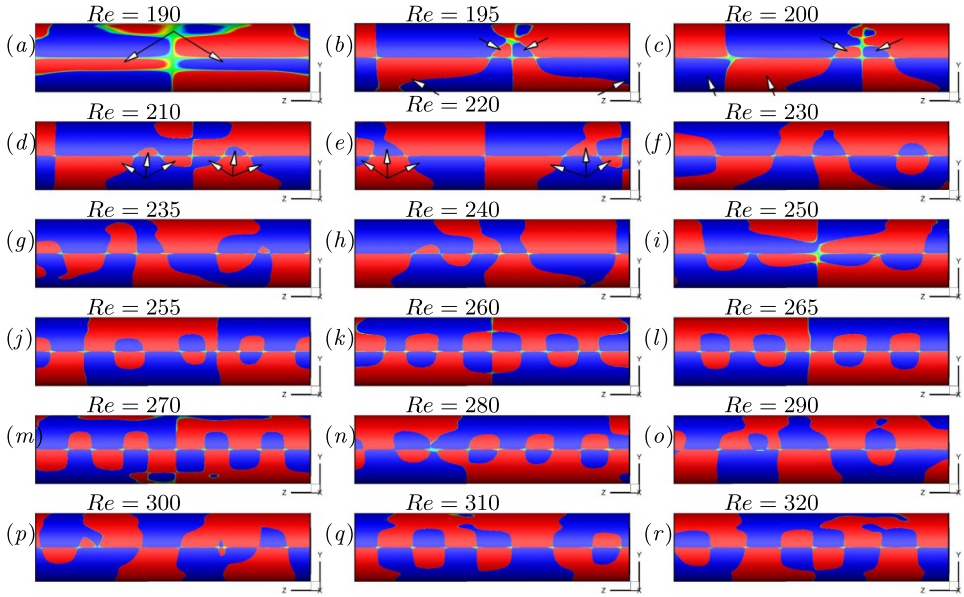

Figure 15. At $t = T_0$ with $L_Z = 4$, contours of ω_x on the rear surface at different Reynolds numbers, where red and blue colors denote positive and negative values, respectively, green color denotes vorticity almost zero ($|\omega_x| < 10^{-3}$), and arrows denote $(\omega_x)_{\mathrm{DA}}$. Particularly, when $\mathrm{Re} \in [230, 240]$, only results with fluid forces at a low level are presented here.

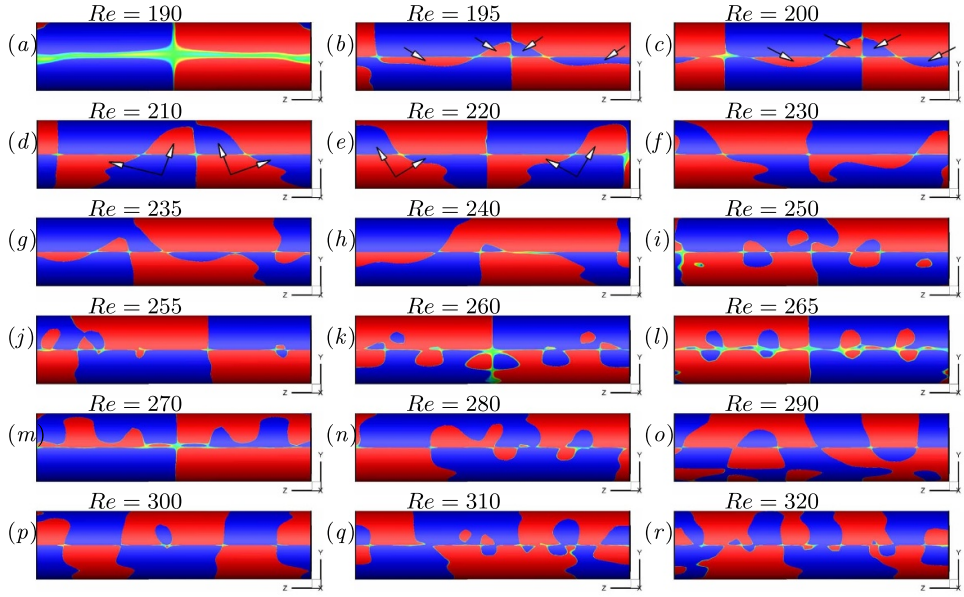

Figure 16. At $t = T_3$ with $L_Z = 4$, contours of ω_x on the rear surface at different Reynolds numbers (same descriptions as in figure 15).

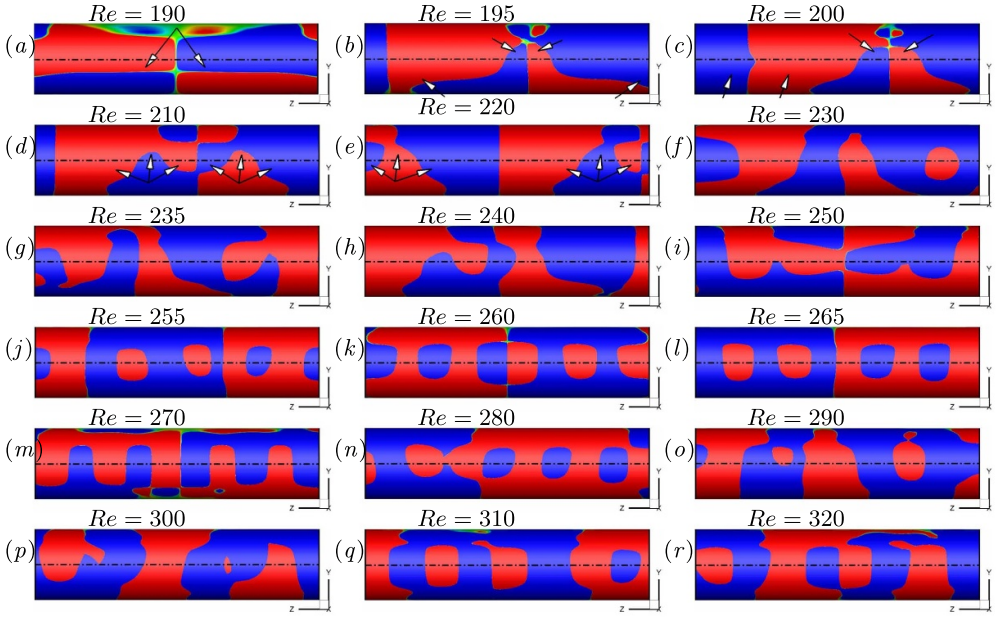

Figure 17. At $t = T_0$ with $L_Z = 4$, contours of ω_y on the rear surface at different Reynolds numbers, where red and blue colors denote positive and negative values, respectively, green color denotes vorticity almost zero ($|\omega_y| < 10^{-3}$), arrows denote $(\omega_y)_{\mathrm{DA}}$, and dotted dash lines denote the center position $y = 0$. Particularly, when $\mathrm{Re} \in [230, 240]$, only results with fluid forces at a low level are presented here.

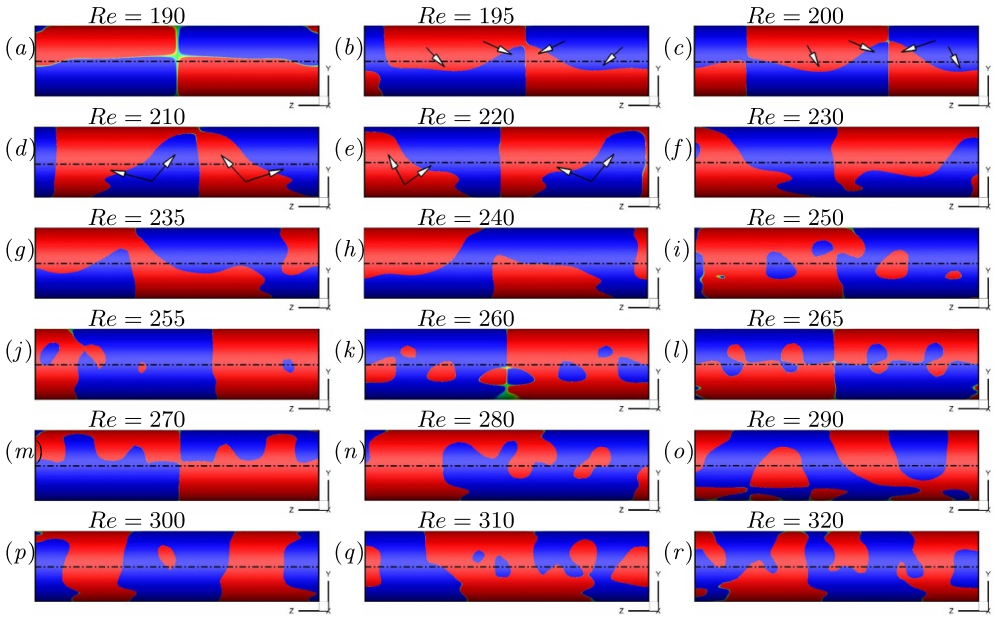

Figure 18. At $t = T_3$ with $L_Z = 4$, contours of ω_y on the rear surface at different Reynolds numbers (same descriptions as in figure 17).

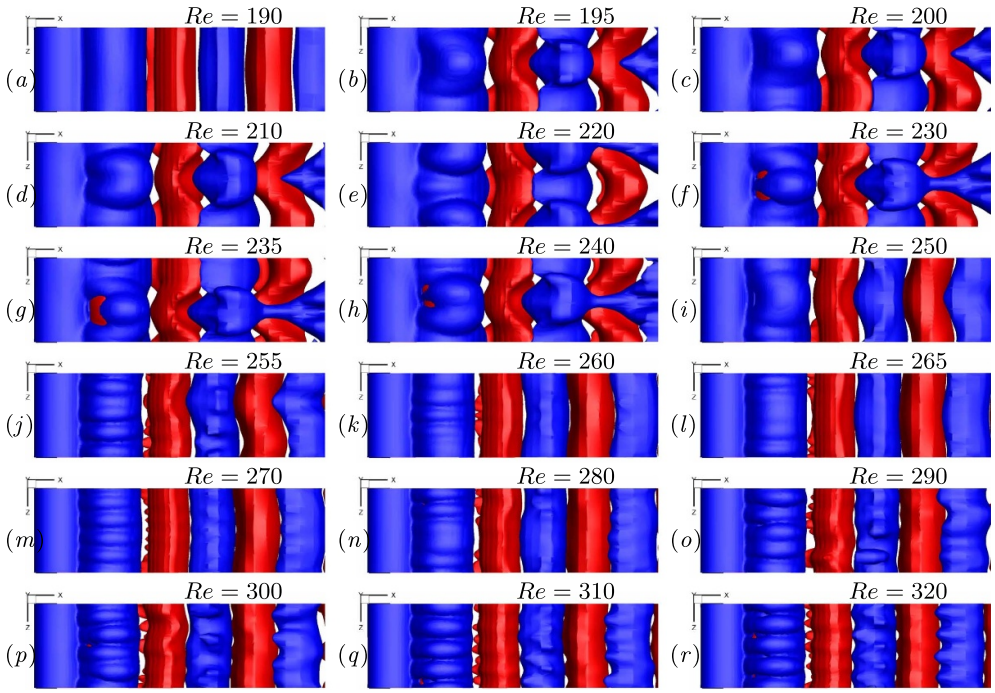

Figure 19. At $t = T_0$ with $L_Z = 4$, top views of isosurfaces of $\omega_z = \pm 0.2$ in the near wake at different Reynolds numbers, where red and blue colors denote positive and negative values, respectively. Particularly, when Re $\in [230, 240]$, only results with fluid forces at a low level are presented here.

shear layers or the near wake when Re exceeds 193 without any effect of vortex dislocations. Therefore, this stage is also referred to as the initially generated stage of pure mode B.

As noted in previous work (Henderson 1997), the Fourier mode with a modulus number of 1 corresponding to (pure) mode A ($\lambda_A = L_Z = 4$ here) is the most unstable modulus in mode competition with different moduli. Moreover, other higher moduli with larger wavenumbers are excited under the strong nonlinear interaction. In the present study, these higher moduli indicate the appearance of wavily ω_{DA}, as well as wavy variation in ω_A, with smaller λ_{DA} or λ_B ($< L_Z$ here) on the rear surface and in the near wake. However, because of these relative weaknesses in ω_{DA} associated with pure mode B, hydrodynamic parameters at Re < 230 still cannot reflect their influence (Lin 2023). Such a phenomenon is similar to the existence of pure mode A in the initial generation stage at Re < 193.

3.4.3. The third stage at $230 \leqslant Re < 260 \sim 265$. In this stage, as reported in our previous work (Lin 2023), there is a gradual transition or mode swapping between pure modes A and B that obviously appears in the near wake. In such mode swapping, there are several vortex-shedding patterns, such as the coexistence of pure modes A and B at different streamwise positions. Two substages are identified based on the characteristics of the fluid forces and vortex-shedding patterns.

In the first substage at Re $\in [230, 240]$, as also reported in previous work (Lin 2023), there are fluid forces at low and high levels, denoted by 'LF' and 'HF', associated with the low and high vortex-shedding frequencies, respectively. Their alternative or intermittent appearance in

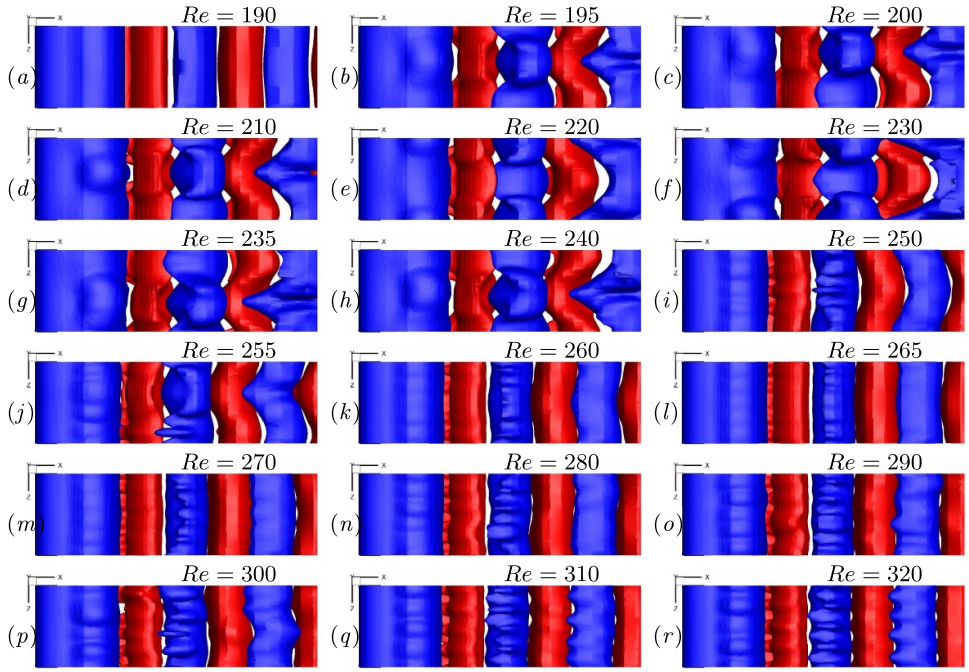

Figure 20. At $t = T_3$ with $L_Z = 4$, top views of isosurfaces of $\omega_z = \pm 0.2$ in the near wake at different Reynolds numbers (same descriptions as in figure 19).

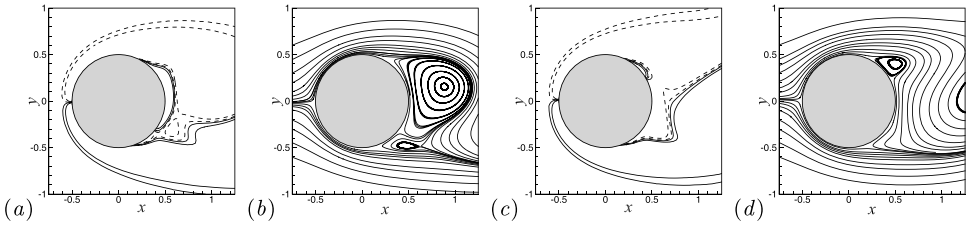

Figure 21. At $z = \frac{1}{4}L_Z$ and Re $= 190$ with $L_Z = 4$, contours of $\omega_z = \pm 0.1$ and ± 0.5 at (a) $t = T_0$ and (c) T_3, and streamlines at (b) $t = T_0$ and (d) T_3 near the rear surface, where solid and dashed lines in contours denote positive and negative values, respectively. Note that the circular-section cylinder is denoted by the grey circle.

the time histories of fluid forces is closely associated with the mode swapping between modes A and B in the near wake.

As shown in figures 11–14, the vortex-shedding patterns at LF are mainly described by pure mode A. Furthermore, as shown in figures 15 and 17, ω_{DA} with the smaller λ_{DA}, which is associated with mode B, still appears partially on the rear surface and in the shear layers, similar to that in the second stage.

However, in the near wake at the HF, there are different vortex-shedding patterns:

(1) Typically, as shown in figures 26–28, only pure mode A appears in the near wake (almost) without any sign of mode B at a certain moment.

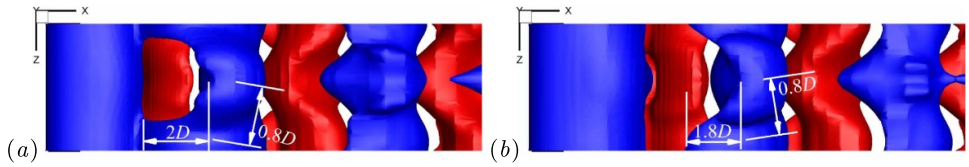

Figure 22. At Re = 195 with $L_Z = 4$, top views of isosurfaces of $\omega_z = \pm 0.2$ in pure mode A at (a) $t = T_1$ and (b) T_2, where red and blue colors denote positive and negative values, respectively. Note that $2D$ or $1.8D$ and $0.8D$ are the distortion spacings along streamwise and vertical directions due to the vertical and streamwise interactions, respectively.

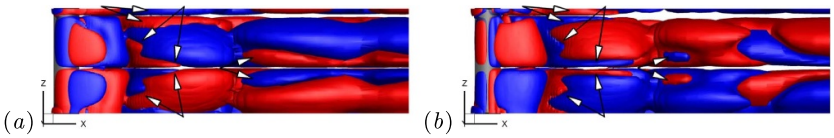

Figure 23. At $t = T_3$, Re = 195 and $L_Z = 4$, bottom views of isosurfaces of (a) $\omega_x = \pm 0.02$ and (b) $\omega_y = \pm 0.02$, where red and blue colors denote positive and negative values, respectively, and arrows at $x < 4$ denote $\pm|\omega_{DA}|$ with $\lambda_{DA} \sim \frac{1}{6}L_Z$ near $z = 1.71$ and 3.7 (see also in figure 6) and $\lambda_{DA} \sim \frac{1}{5}L_Z$ elsewhere. Note that the cylinder is denoted by the grey translucent surface and the flow is from left to right.

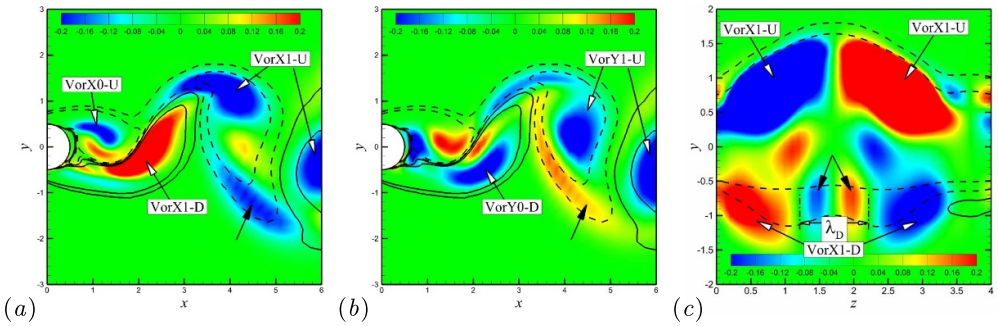

Figure 24. At $t = T_0$, Re = 195 and $L_Z = 4$, contours of (a) ω_x and (b) ω_y at $z = 1.46$, and (c) ω_x at $x = 4$, where solid and dashed contour lines of $\omega_z = \pm 0.1$ and ± 0.5 denote positive and negative values, respectively, and arrows with black filled arrowheads denote $\pm|\omega_{DA}|$ with $\lambda_{DA} \sim \frac{1}{4}L_Z$.

(2) At other moments, the mixed mode occurs. For example, as shown in figure 29, pure mode A is dominant, but some features in mode B also appear in the shear layers and the first shedding primary vortex, similar to the case at Re < 230. As shown in figure 30, modes A and B coexist at different streamwise positions, and wavy features with smaller spanwise wavelengths due to mode B obviously appear in the shear layers. As shown in figure 31, pure mode B mainly exists in the shear layers and the first shedding primary vortex, while pure mode A mainly appears in the near wake of $x > 5.5 \sim 7.5$.

(3) Sometimes, as shown in figure 32, only pure mode B with $\lambda_B = \frac{1}{5}L_Z$ exists in the near wake.

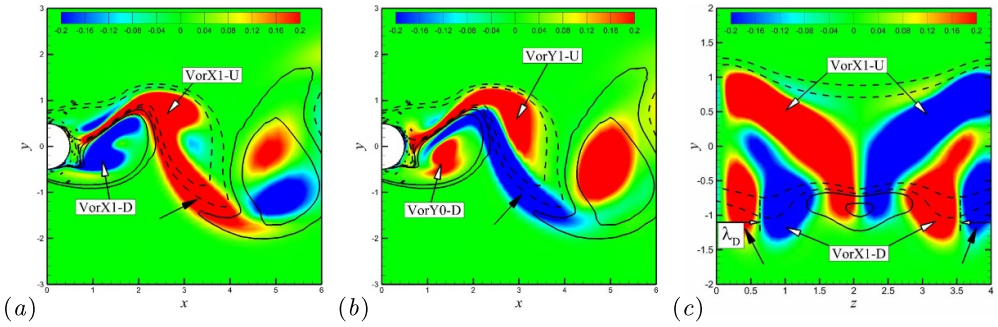

Figure 25. At $t = T_3$, Re $= 220$ and $L_Z = 4$, contours of (a) ω_x and (b) ω_y at $z = 0.3$, and (c) ω_x at $x = 3$ (same descriptions as in figure 24).

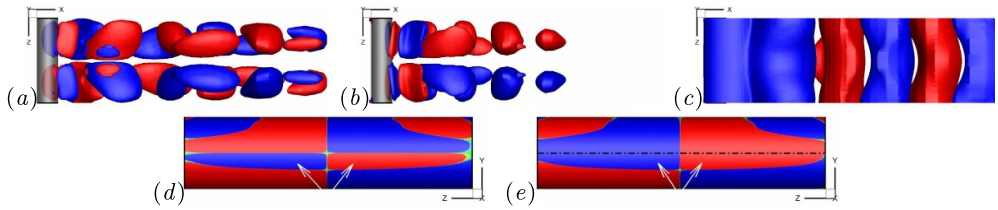

Figure 26. At $t = 1865.5$ (T_0) (HF), top views of isosurfaces of (a) $\omega_x = \pm 0.1$, (b) $\omega_y = \pm 0.1$ and (c) $\omega_z = \pm 0.2$ in the near wake at Re $= 230$ with $L_Z = 4$, and contours of (d) ω_x and (e) ω_y on the rear surface, where red and blue colors denote positive and negative values, respectively, and green color in contours denotes $|\omega| < 10^{-3}$, and arrows denote ω_{DA} with $\lambda_{DA} = L_Z$, just as in figure 5. Note that the cylinder is denoted by the grey translucent surface and the flow is from left to right in isosurfaces.

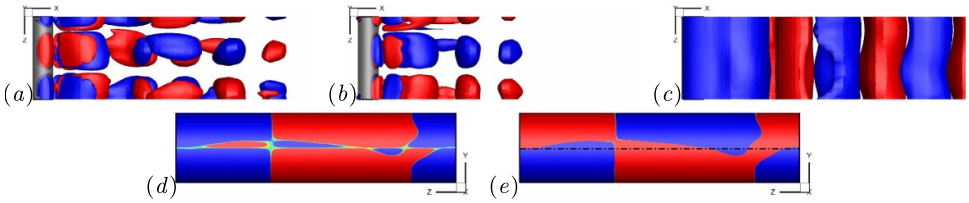

Figure 27. At $t = 2242$ (T_3) (HF), top views of isosurfaces of (a) $\omega_x = \pm 0.1$, (b) $\omega_y = \pm 0.1$ and (c) $\omega_z = \pm 0.2$ in the near wake at Re $= 235$ with $L_Z = 4$, and contours of (d) ω_x and (e) ω_y on the rear surface (same descriptions as in figure 26).

Meanwhile, for vorticity distributed on the rear surface at HF, mainly in the mixed mode and only pure mode B as stated above in figures 29–32, ω_{DA} associated with mode B at $|y| < 0.17 \sim 0.3$ is also in a gradual transition: distribution only on one side of $y = 0$ to that on both sides at the same spanwise position mainly with $\lambda_B < L_Z$, therefore satisfying the sign relationship equation (3.6). Particularly, in the case of the mixed mode, there is a new transitional phenomenon in which ω_{DA} with different λ_{DA} varying from λ_B to L_Z still satisfies the sign relationship of pure mode B in equation (3.6), e.g. at $|y| > 0.17 \sim 0.27$ in figures 29 and 30 and $|y| \leqslant 0.5$ in figure 31, referred to as the wavelength modulation of pure mode B. The occurrence of this phenomenon only interferes with and even inhibits the generation of

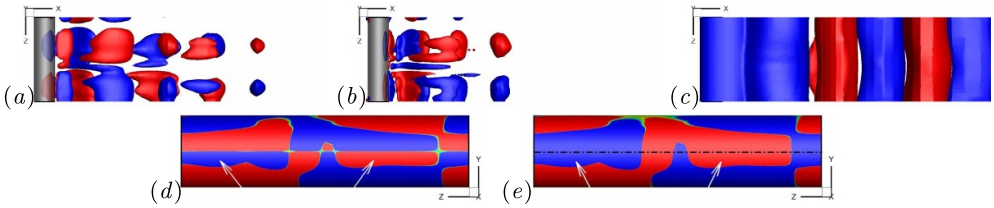

Figure 28. At $t = 2044.5$ (T_0) (HF), top views of isosurfaces of (a) $\omega_x = \pm 0.1$, (b) $\omega_y = \pm 0.1$ and (c) $\omega_z = \pm 0.2$ in the near wake at Re $= 240$ with $L_Z = 4$, and contours of (d) ω_x and (e) ω_y on the rear surface (same descriptions as in figure 26).

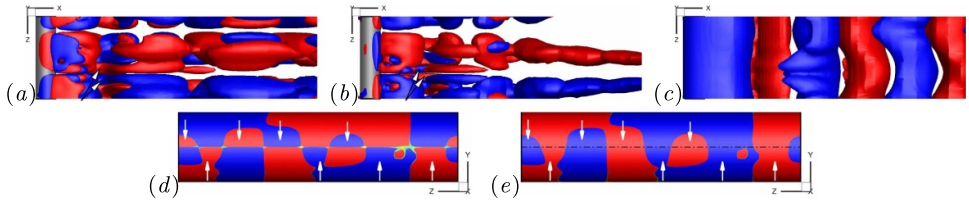

Figure 29. At $t = 2210.5$ (T_2) (HF), top views of isosurfaces of (a) $\omega_x = \pm 0.1$, (b) $\omega_y = \pm 0.1$ and (c) $\omega_z = \pm 0.2$ in the near wake at Re $= 235$ with $L_Z = 4$, and contours of (d) ω_x and (e) ω_y on the rear surface, where arrows with hollow arrowheads denote the appearance of mode B with λ_B approximately $0.8 \sim 0.9$, and arrows with filled arrowheads denote ω_{DA} on the rear surface mainly due to mode B.

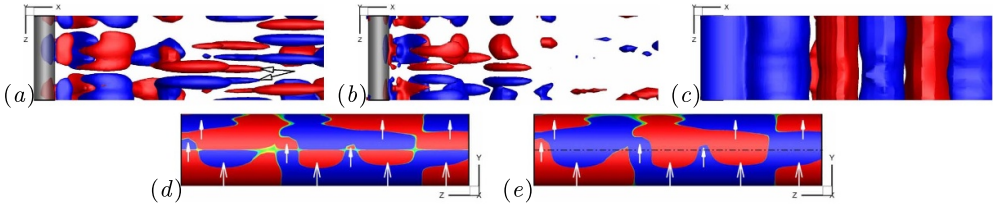

Figure 30. At $t = 2401$ (T_0) (HF), top views of isosurfaces of (a) $\omega_x = \pm 0.1$, (b) $\omega_y = \pm 0.1$ and (c) $\omega_z = \pm 0.2$ in the near wake at Re $= 235$ with $L_Z = 4$, where arrows with hollow arrowheads denote the appearance of mode B with λ_B approximately 1, and contours of (d) ω_x and (e) ω_y on the rear surface, where arrows with filled arrowheads denote ω_{DA} due to mode B, while arrows with plain arrowheads denote ω_{DA} owing to pure mode A, like that in figure 5.

ω_A on and near the rear surface, even in the braid shear layers. However, in the case of only pure mode B, some sign features in pure mode A are only demonstrated in a local region on the rear surface, i.e. equation (3.3) at $|y| > 0.3$.

In the second substage at $240 < Re < 260 \sim 265$, as presented in previous work (Lin 2023), only fluid forces at a high level with a high vortex-shedding frequency exist in the time histories. For the vortex-shedding pattern, typically as shown in figures 11 and 12, the above mixed mode still exists. For example, at Re $= 250$ and $t = T_0$, pure mode A is obviously dominant in the alternately shedding primary vortices. In the shear layers, there is ω_{DA} with smaller λ_{DA}. At $t = T_3$, in the shear layers and first shedding primary vortex, pure mode B with $\lambda_B = 1$ is dominant, while some features in pure mode A remain further downstream. However, at Re $= 255$,

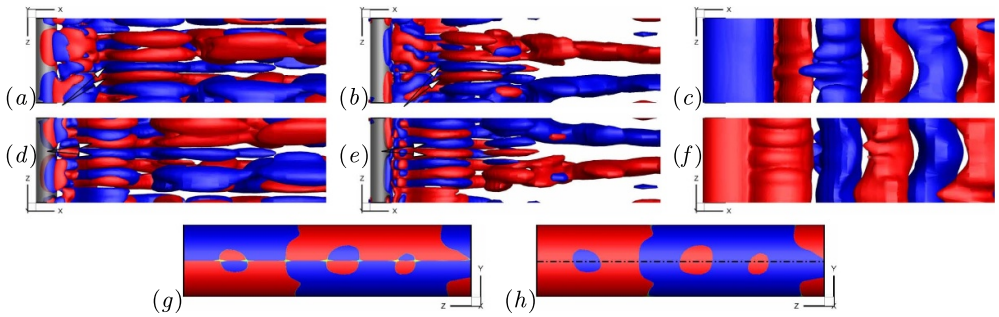

Figure 31. At $t = 1876.5$ (T_2) (HF), top views of isosurfaces of (a) $\omega_x = \pm 0.1$, (b) $\omega_y = \pm 0.1$ and (c) $\omega_z = \pm 0.2$, where arrows denote the appearance of mode B with λ_B approximately 1, and bottom views of isosurfaces of (d) $\omega_x = \pm 0.1$, (e) $\omega_y = \pm 0.1$ and (f) $\omega_z = \pm 0.2$ in the near wake at Re $= 240$ with $L_Z = 4$, and contours of (g) ω_x and (h) ω_y on the rear surface.

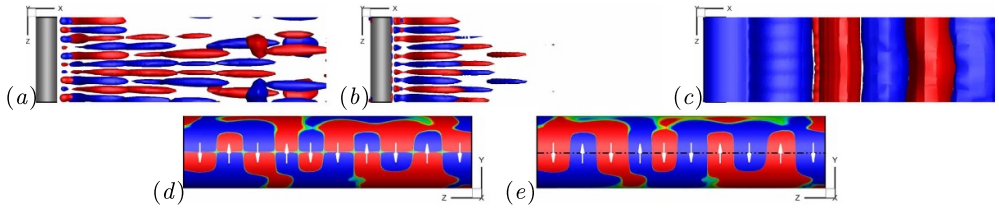

Figure 32. At $t = 2415.5$ (T_0) (HF), top views of isosurfaces of (a) $\omega_x = \pm 0.1$, (b) $\omega_y = \pm 0.1$ and (c) $\omega_z = \pm 0.2$ in the near wake at Re $= 240$ with $L_Z = 4$, and contours of (d) ω_x and (e) ω_y on the rear surface, where arrows denote ω_{DA} caused by mode B with $\lambda_B \sim 0.8$.

the above characteristics are opposite, i.e. mode A dominant in the shedding primary vortices at $t = T_3$ and mode B dominant in the shear layers at $t = T_0$.

For vorticity distributed on the rear surface, as shown in figures 15–18, similar features in the first substage (the mixed mode) at HF stated above are still valid here. For example, at $t = T_0$, ω_{DA} due to mode B is distributed mainly on one side of $y = 0$ at Re $= 250$ and then on both sides at Re $= 255$, at which ω_A mainly exists in the local region $|y| > 0.25$. Particularly, on the whole rear surface $|y| \leqslant 0.5$, the wavelength modulation of pure mode B also occurs at T_0 when $255 \leqslant Re \leqslant 265$ and T_3 when $250 \leqslant Re \leqslant 260$. At this point, the physical mechanism in the formation of pure mode A in the wall and shear layers is completely disturbed or even suppressed.

3.4.4. The fourth stage at Re $\geqslant 260 \sim 265$. In this stage, as shown in figures 11–14, the near wake is always described by pure mode B with λ_B of $\frac{1}{5}L_Z = 0.8$ at Re < 290 and $\frac{1}{4}L_Z = 1$ at Re $\geqslant 310$. Interestingly, at $290 \leqslant Re < 310$, pure mode B coexists with two different wavelengths, such as approximately 0.89 at $t = T_0$ and Re $= 290$ and 300, but approximately 0.8 at $t = T_3$ and Re $= 290$ and 1 at Re $= 300$. As shown in figure 33, the wavy spanwise vortex is mainly attributed to this streamwise interaction (Meiburg and Lasheras 1988, Lin and Tan 2022).

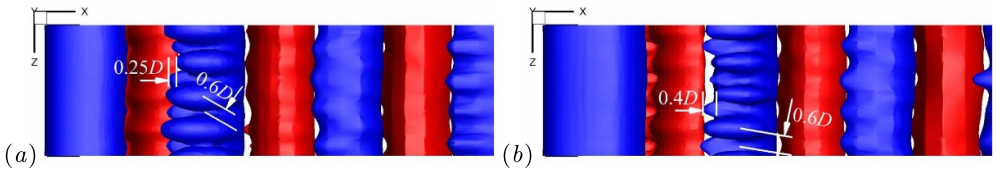

Figure 33. At Re = 310 with $L_Z = 4$, top views of isosurfaces of $\omega_z = \pm 0.2$ in pure mode B at (a) $t = T_1$ and (b) T_2, where red and blue colors denote positive and negative values, respectively. Note that $0.25D$ or $0.4D$ and $0.6D$ are the distortion spacings along streamwise and vertical directions due to the vertical and streamwise interactions, respectively.

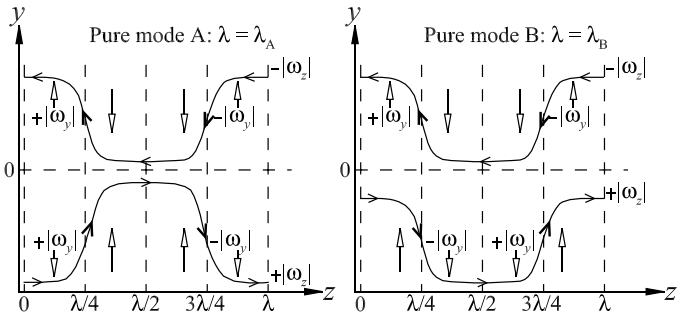

Figure 34. Sketches of vortex lines for pure modes A and B projected in the (y, z) plane, where arrows with hollow arrowheads denote the spanwise vortex distorted along the y-axis.

For the vorticity distribution on the rear surface, typically as shown in figures 15 and 17, similar features at $t = T_0$ are presented. In the first feature, at Re < 290 and Re > 300, the vorticity sign relationship of pure mode B, equation (3.6), becomes dominant and is mainly distributed on both sides of $y = 0$ at the same spanwise position, while the vorticity sign relationship equation (3.3), as ω_{DB}, is only in the local region, e.g. $|y| > 0.3$. In the second feature, at $290 \leqslant Re \leqslant 300$, there is a mixed case: at a certain spanwise position, ω_{B} extends to $y = \pm 0.5$; or at other spanwise position, ω_{B} confined in the region approximately $|y| < 0.33$ coexists with ω_{DB} in the region $|y| > 0.33$.

3.4.5. Spanwise phase change in pure modes A and B. As reported in previous works (Lin *et al* 2018a, Lin and Tan 2022, Lin and Wu 2022), pure modes A and B can be described by alternately shedding Π_- and Π_+ vortices. In the Π-type vortex, the head '—' denotes the (wavy) spanwise vortex, while the two legs '||' denote additional vorticities with the spanwise wavelength λ. Among them, the Π_- vortex is defined as the following vorticity sign combinations, $(+|\omega_x|, +|\omega_y|, -|\omega_z|)$ at $z = \frac{1}{4}\lambda$ and $(-|\omega_x|, -|\omega_y|, -|\omega_z|)$ at $z = \frac{3}{4}\lambda$, originally shedding from the upper shear layer. The Π_+ vortex is defined by the following vorticity sign combinations, $(-|\omega_x|, +|\omega_y|, +|\omega_z|)$ at $z = \frac{1}{4}\lambda$ and $(+|\omega_x|, -|\omega_y|, +|\omega_z|)$ at $z = \frac{3}{4}\lambda$, originally shedding from the lower shear layer. Generally, when $\lambda = \lambda_{\mathrm{A}}$, these Π_- and Π_+ vortices alternately shedding in phase across the span can be used to describe the pure mode A, i.e. $(+|\omega_x|, +|\omega_y|, -|\omega_z|)$ and $(-|\omega_x|, +|\omega_y|, +|\omega_z|)$ at the same spanwise position or $z = \frac{1}{4}\lambda_{\mathrm{A}}$ here. However, when $\lambda = \lambda_{\mathrm{B}}$, pure mode B can be illustrated by Π_- and Π_+ vortices alternately shedding out of phase across the span, i.e. $(+|\omega_x|, +|\omega_y|, -|\omega_z|)$ and $(+|\omega_x|, -|\omega_y|, +|\omega_z|)$ at the same spanwise position or $z = \frac{1}{4}\lambda_{\mathrm{B}}$. As shown in figure 34, based on the streamwise

interaction (Meiburg and Lasheras 1988), the term 'in phase' in pure mode A indicates that the direction of primary vortex distortion detached from the upper and lower shear layers points to the position of $y = 0$ (the wake center plane) at the same spanwise position, while the term 'out of phase' in pure mode B illustrates that the distortion direction of alternately shedding spanwise vortices points to $y = 0$ at different spanwise positions with a spanwise phase difference of $\lambda_B/2$.

According to the above analysis, especially in the second stage at $193 \leqslant Re < 230$ and the third stage at $230 \leqslant Re < 260 \sim 265$, the spanwise phase change from the originally dominant pure mode A to the gradual appearance of pure mode B as a kind of disturbance is explained as follows:

(1) At the 'end' spanwise position, such as $(y = 0, z = 1.71)$ in figure 6(a), near which ω_A is weak (almost disappears), any disturbance can easily lead to the generation of ω_{DA}.
(2) After ω_{DA} is generated, its sign is exactly opposite to that of ω_A, and its λ_{DA} is almost similar to λ_B at high Reynolds numbers, which indicates that the modulus of pure mode B appears partially on the rear surface. Note that the above two points are supported by similar analysis in appendix A, such as the appearance of ω_{DA} near $z = 2$ in figures 38(b) and (d).
(3) A similar phenomenon with opposite signs between ω_A and ω_{DA} also occurs in the near wake. For example, as shown in figures 23–25, at the same spanwise position, there is a dominant distribution with $(+|(\omega_x)_A|, +|(\omega_y)_A|, -|\omega_z|)$ in the upper shear layer due to pure mode A and a disturbance distribution with $(+|(\omega_x)_{DA}|, -|(\omega_y)_{DA}|)$ owing to mode B, instead of the distribution with $(-|(\omega_x)_A|, +|(\omega_y)_A|)$ in pure mode A. Moreover, such ω_{DA} moves into the lower side of the wake center plane, as shown by arrows in the far wake in figure 23.
(4) For these ω_{DA}, although λ_{DA} is mainly determined by pure mode B, the Π_- and Π_+ vortices near the 'end' positions alternately shed in phase across the local span until Re is less than $235 \sim 240$, such as $z \sim 1.71$ at $Re = 195$ and $z \sim 1.25$ at $Re = 200$, as shown in figures 23 and 11. Meanwhile, at the 'middle' positions, ω_A is gradually disturbed in both time and space by those ω_{DA} associated with pure mode B. Then, as the wavelength modulation of pure mode B on the rear surface finally appears in the mixed mode when Re exceeds $235 \sim 240$, the Π_- and Π_+ vortices with λ_B alternately shed out of phase, as shown in figure 31. This process appears to be the spanwise expansion of pure mode B first near the 'end' positions and then at the 'middle' positions. The spanwise phase transition is basically completed.
(5) When Re increases from 195 to 265, ω_{DA} associated with pure mode B appears on both sides of $y = 0$ on the rear surface and also in both the upper and lower shear layers at the same spanwise position.

3.5. Critical Reynolds numbers

As stated in previous work (Lin 2023) and the above analysis, it is not entirely appropriate to use the $St - Re$ relationship to determine the critical Reynolds number at which mode B occurs in different stages. This limitation occurs because at high Reynolds numbers, the coexistence

of pure modes A and B is observed in the near wake, as is the appearance of mode A through time histories with high levels of fluid forces and high vortex-shedding frequency.

Based on the RMS lift coefficient over time, some definitions of vorticity intensities on the basis of volume integrals proposed in previous work (Lin 2022) are adopted as follows. The volume-averaged streamwise and vertical vorticities, $\overline{\omega}_x$ and $\overline{\omega}_y$, respectively, and the volume-RMS streamwise vorticity, ω_x', volume-RMS vertical vorticity, ω_y', and volume-RMS additional vorticity, ω_{xy}', are defined as:

$$\overline{\omega}_x(t) = \frac{1}{V}\int_V \omega_x \mathrm{d}\tau \approx 0, \tag{3.20a}$$

$$\overline{\omega}_y(t) = \frac{1}{V}\int_V \omega_y \mathrm{d}\tau \approx 0, \tag{3.20b}$$

$$\omega_x'(t) = \sqrt{\frac{1}{V}\int_V (\omega_x - \overline{\omega}_x)^2 \mathrm{d}\tau} \approx \sqrt{\frac{1}{V}\int_V \omega_x^2 \mathrm{d}\tau}, \tag{3.21a}$$

$$\omega_y'(t) = \sqrt{\frac{1}{V}\int_V (\omega_y - \overline{\omega}_y)^2 \mathrm{d}\tau} \approx \sqrt{\frac{1}{V}\int_V \omega_y^2 \mathrm{d}\tau}, \tag{3.21b}$$

$$\omega_{xy}'(t) = \sqrt{\frac{1}{V}\int_V \left[(\omega_x - \overline{\omega}_x)^2 + (\omega_y - \overline{\omega}_y)^2\right] \mathrm{d}\tau} = \sqrt{\omega_x'^2 + \omega_y'^2} \tag{3.21c}$$

where V is the volume of the flow field of interest (i.e. the whole computational domain) and $\mathrm{d}\tau$ is the volume element. The volume integral includes all possible moduli associated with pure modes A and B appearing in the whole wake.

Using the above variables and the aforementioned vortex shedding phenomena, the following critical Reynolds numbers in both pure modes A and B can be obtained.

Through precise computations with a small calculated interval of the Reynolds number, δRe, there are two critical Reynolds numbers in pure mode A, as shown in figure 35. The first critical Reynolds number, $\mathrm{Re}_{\mathrm{Acr0}}$, is 141 (± 0.5) with $\delta Re = 1$. This indicates that natural three dimensionality first appears on the cylinder surface, particularly on the rear surface near the wake center plane $y = 0$. This intrinsic three dimensionality leads to the generation of additional vorticities on the rear surface. The spanwise wavelength of these surface vorticities is the same as that of pure mode A, i.e. $\lambda_{\mathrm{A}} = 4$. The second critical Reynolds number, $\mathrm{Re}_{\mathrm{Acr1}}$, is 193 (± 0.5) with $\delta Re = 1$, which indicates the fully developed stage of pure mode A in the near wake (Lin 2022, 2023).

However, for mode B, computations with different L_Z are executed, as shown in figure 35. When $L_Z = 1$, there is only one stage in which pure mode B appears with the critical Reynolds numbers $\mathrm{Re}_{\mathrm{Bcr}}$ of 299. However, when $L_Z = 4$, based on the above vorticity analysis, there are at least four stages. As shown in figure 35, the first critical Reynolds number $\mathrm{Re}_{\mathrm{Bcr0}} = 193$ (± 0.5) indicates that pure mode B is initially generated in the flow. The three volume-RMS vorticities gradually increase when $193 \leqslant Re < 230$. The second critical Reynolds number $\mathrm{Re}_{\mathrm{Bcr1}} = 230$ (± 2.5) indicates that the appearance of mode B has an important effect on fluid forces and vortex-shedding frequency in a gradual transition or mode swapping. All volume-RMS vorticities wavily decrease when $230 \leqslant Re < 260 \sim 265$ until pure mode A totally disappears in the near wake, as shown in figure 35. The third critical Reynolds number $\mathrm{Re}_{\mathrm{Bcr2}} =$

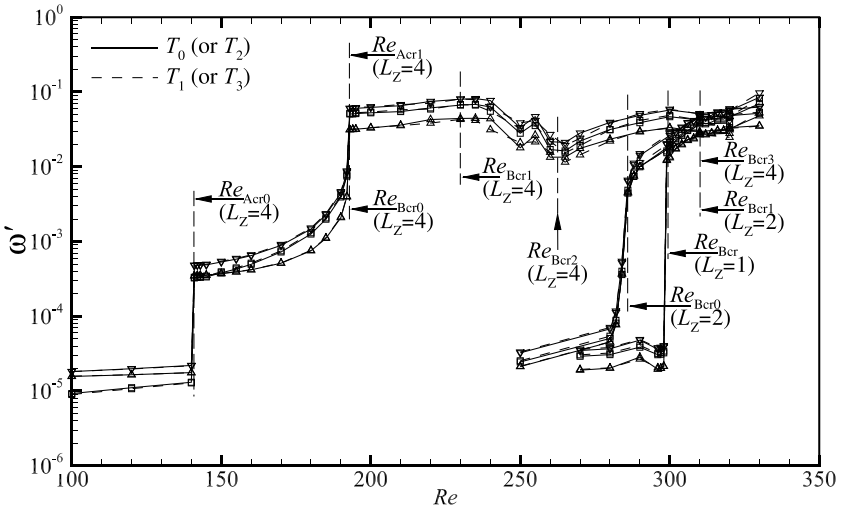

Figure 35. Relationship between the volume-RMS vorticity and Reynolds number, where symbols of □, △ and ▽ denote ω_x', ω_y' and ω_{xy}' expressed by equation (3.21), respectively, based on figures 11–14.

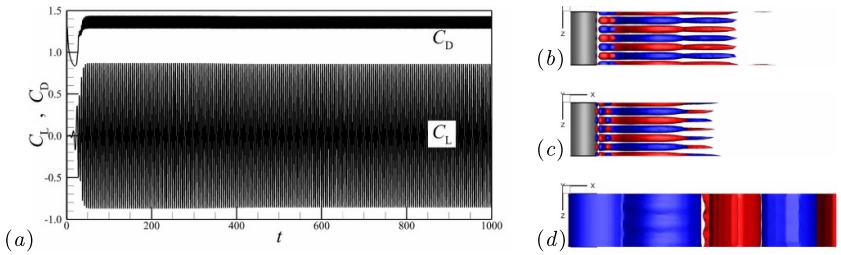

Figure 36. At Re = 290 with $L_Z = 2$, (a) time histories of fluid forces and top views of isosurfaces of (b) $\omega_x = \pm 0.1$, (c) $\omega_y = \pm 0.1$ and (d) $\omega_z = \pm 0.2$ in pure mode B at $t = 996$ (T_0), where red and blue colors denote positive and negative values, respectively. Note that the cylinder is denoted by the grey translucent surface and the flow is from left to right in isosurfaces.

262.5 (± 2.5) indicates that pure mode B is in a stage of self-adjustment of λ_B from 0.8 to 1. When $265 \leqslant Re < 310$, volume-RMS vorticities gradually increase. Interestingly, a similar phenomenon also appears with $L_Z = 2$, in which λ_B varies from $2/3$ at $286 \leqslant Re < 310$ to 1 at Re = 310, as shown in figures 36 and 37. The fourth critical Reynolds number $Re_{Bcr3} = 310$ (± 5) indicates that pure mode B is fully developed with $\lambda_B = 1$, which is consistent with those at $L_Z = 1$ and 2 in the variation of volume-RMS vorticities, as shown in figure 35 at Re $\geqslant$ 310.

Moreover, from the perspective that pure mode B appears in the entire near wake, it is appropriate that Re_{Bcr} can be determined by Re_{Bcr2}, which agrees with the values of 259 and 261 (± 0.2) predicted by Barkley and Henderson (1996) and Posdziech and Grundmann (2001), respectively. Then, as L_Z increases, Re_{Bcr} gradually decreases, i.e. 299 ($L_Z = 1$), 286 ($L_Z = 2$) and 262.5 ($L_Z = 4$). This feature shows that with the gradual relaxation of the periodic constraint, that is, the gradual increase of finite L_Z, the Fourier mode corresponding to pure mode B for the entire wake becomes more easily excited at lower Reynolds numbers.

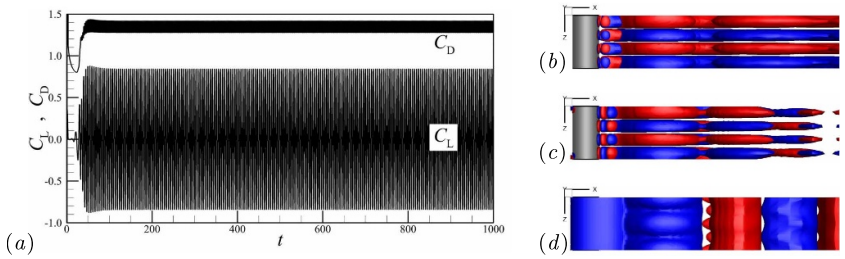

Figure 37. At Re = 310 with $L_Z = 2$, (a) time histories of fluid forces and top views of isosurfaces of (b) $\omega_x = \pm 0.1$, (c) $\omega_y = \pm 0.1$ and (d) $\omega_z = \pm 0.2$ in pure mode B at $t = 996.5$ (T_0) (same descriptions as in figure 36).

4. Conclusions

In this paper, the spanwise phase transition from pure mode A to mode B in the wake of a circular cylinder is investigated through DNS in the absence of vortex dislocations. As the second part of this study, the spatiotemporal evolution of the vorticity on the rear surface of the cylinder and in the near wake is illustrated in the Re range from 190 to 330 with a computational spanwise length L_Z of 4.

By comparing the features of the vorticity signs in pure modes A and B, relevant spanwise phase transitions are determined as follows:

(1) For pure mode A with wavelength $\lambda_A = 4$, the first critical Reynolds number $\mathrm{Re}_{\mathrm{Acr0}}$ is 141 (± 0.5). When Re exceeds $\mathrm{Re}_{\mathrm{Acr0}}$ as the initially generated stage, the three dimensionality associated with pure mode A appears first on the rear surface, then in the shear layers and finally in the alternately shedding primary vortices (Lin 2022). The second critical Reynolds number $\mathrm{Re}_{\mathrm{Acr1}}$ is 193 (± 0.5). When $\mathrm{Re} \geqslant Re_{\mathrm{Acr1}}$, pure mode A is in the fully developed stage. The Π_- and Π_+ vortices associated with mode A alternately shed in phase across the span.

(2) For pure mode B, the first critical Reynolds number $\mathrm{Re}_{\mathrm{Bcr0}}$ is 193 (± 0.5). When $\mathrm{Re} \geqslant Re_{\mathrm{Bcr0}}$ at the initially generated stage, some features of the vorticity sign in mode B, as a type of weak disturbed vorticity with opposite signs in a wavelength range from approximately $\frac{1}{6}L_Z$ to $\frac{1}{3}L_Z$, partially appear on the rear surface and in the shear layers near the 'end' positions. At a certain spanwise position, a part of mode A and a part of mode B coexist, e.g. the Π_- vortex in mode A and the Π_+ vortex with specific signs in mode B. The Π_- and Π_+ vortices associated with mode B alternately shed in phase across the span, exactly the same as those in pure mode A. The second critical Reynolds number $\mathrm{Re}_{\mathrm{Bcr1}}$ is approximately 230 (± 2.5). When Re exceeds $\mathrm{Re}_{\mathrm{Bcr1}}$, a gradual increase in additional vorticities in mode B leads to mode swapping, such as modes A and B coexisting at different streamwise or spanwise positions. With the appearance of the wavelength modulation of pure mode B at the 'middle' positions, the Π_- and Π_+ vortices associated with mode B alternately shed out of phase across the span. The third critical Reynolds number $\mathrm{Re}_{\mathrm{Bcr2}}$ is approximately 262.5 (± 2.5). When $\mathrm{Re} \geqslant Re_{\mathrm{Bcr2}}$, pure mode B is dominant in the near wake. The resulting spanwise wavelength λ_B is gradually changed from 0.8 to 1. The fourth critical Reynolds number $\mathrm{Re}_{\mathrm{Bcr3}}$ is approximately 310 (± 5). When $\mathrm{Re} \geqslant Re_{\mathrm{Bcr3}}$, pure mode B is in the fully developed stage with $\lambda_B = 1$, which is well consistent with that with $L_Z = 1$ and 2.

In our future works, the effect of vortex dislocations on this spanwise phase transition will be further investigated.

Acknowledgments

The authors wish to thank the Hainan Province Science and Technology Special Fund (ZDYF2022GXJS004, ZDYF2021GXJS028) for this work.

Conflict of interest

The authors report no conflict of interest.

Appendix A. Analysis of vorticity with λ_A and λ_{DA} at $Re < 230$

Here, to illustrate the physical relationship between the spanwise waviness in the vorticity ω (i.e. ω_x or ω_y) isosurface and the spanwise wavelength of additional vorticities associated with pure modes A and B, a qualitative analysis is carried out. The reason is that it is difficult to distinguish and display ω_A and ω_{DA} in the vorticity isosurfaces individually. Therefore, a simple superposition of vorticity with different spanwise wavelengths is adopted.

Without losing generality or for the convenience of simplicity, some preconditions are assumed or prescribed as follows:

(1) Only two wavelengths are taken into account, although there are many other moduli appearing in the spatiotemporal evolution due to nonlinear interactions.
(2) Two different spanwise wavelengths are λ_A and λ_{DA} due to pure modes A and B, respectively.
(3) ω_A with $\lambda_A = 4$ is dominant, while ω_{DA} with λ_{DA} from $\frac{1}{6}L_Z$ to $\frac{1}{3}L_Z$ is subordinate when $L_Z = 4$. Here, the modulus m of ω_{DA} is defined as $m = L_Z/\lambda_{DA}$. Consequently, $m = 3, 4, 5$ and 6 are considered based on the aforementioned analysis of the spatiotemporal evolution of vorticity.
(4) Therefore, the vorticity ω showing the spanwise waviness feature is assumed to be the linear superposition of vorticities ω_A and ω_{DA}, i.e. $\omega = \omega_A + \omega_{DA}$.
(5) As shown in figure 3 or 4 at $Re < 230$, the spanwise variation in ω_A with opposite signs can be expressed by the periodic sine function, i.e. $\omega_A = a_A \sin(\frac{2\pi z}{\lambda_A})$, where a_A is the peak amplitude of ω_A across the span.
(6) Due to the unknown variation in ω_{DA} with λ_{DA}, two possible distributions are assumed first, i.e. $\omega_{DA} = a_{DA} \sin(\frac{2\pi z}{\lambda_{DA}})$ and $a_{DA} \cos(\frac{2\pi z}{\lambda_{DA}})$ without the spanwise phase difference from ω_A, where a_{DA} is the peak amplitude of ω_{DA} across the span. Furthermore, as shown in figure 4, at specific spanwise positions, $\omega = \omega_x = \omega_y = 0$. Accordingly, at $z = 0$ and $\frac{1}{2}\lambda_A = 2$, $\omega_A = 0$, but $\omega_{DA} = a_{DA} \cos(\frac{2\pi z}{\lambda_{DA}}) = a_{DA} \cos(\frac{2\pi mz}{L_Z}) \neq 0$, which leads to $\omega \neq 0$. As a result, only sinusoidal variation in ω_{DA} is analyzed.
(7) To be consistent with the analysis of the phase transition, two positions, $z = 0$ or $\lambda_A = 4$ and $\frac{1}{2}\lambda_A = 2$, are defined as the 'end' positions in figure 6 or 23, while the spanwise positions, i.e. $0 < z < 2$ and $2 < z < 4$, are defined as the 'middle' positions.

As shown in figures 38 and 39, ω_{DA} with the present moduli results in the intensity of ω varying across the span. By comparing figures 4 and 23 or 11 and 13, there are two situations in the spanwise waviness of vorticity isosurfaces at the 'middle' positions, typically as shown in

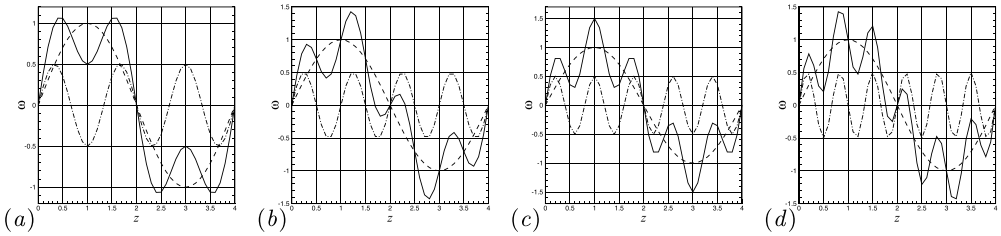

Figure 38. Amplitudes of ω, ω_{A} with $a_{\mathrm{A}} = 1$ and ω_{DA} with $a_{\mathrm{DA}} = 0.5$ along the spanwise direction with different moduli (a) $m = 3$, (b) 4, (c) 5 and (d) 6, where solid lines (—), dashed lines ($-\ -\ -$) and dotted-dash lines ($-\cdot-$) denote ω, ω_{A} and ω_{DA}, respectively.

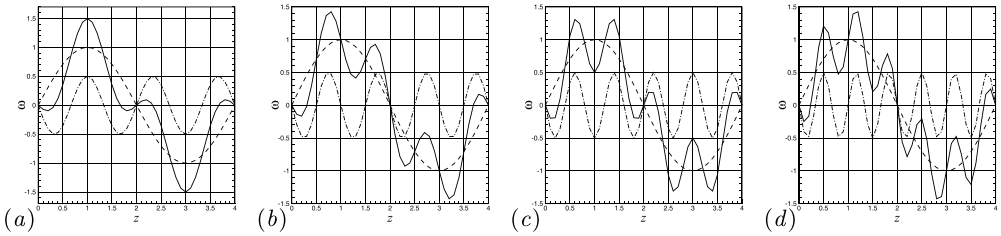

Figure 39. Amplitudes of ω, ω_{A} with $a_{\mathrm{A}} = 1$ and ω_{DA} with $a_{\mathrm{DA}} = -0.5$ along the spanwise direction with different moduli (a) $m = 3$, (b) 4, (c) 5 and (d) 6, where solid lines (—), dashed lines ($-\ -\ -$) and dotted-dash lines ($-\cdot-$) denote ω, ω_{A} and ω_{DA}, respectively.

figure 23(b). The first is the one 'W'-like wavy shape in the ω (e.g. ω_{y}) isosurfaces, except the boundary of ω with a constant sign near the two 'end' positions. Only the case in figure 38(c) can reflect such 'W'-like waviness with this boundary. The second is the one 'V'-like wavy shape in the ω isosurfaces. If the condition that $\mathrm{sgn}(\omega_{\mathrm{DA}}) = -\mathrm{sgn}(\omega_{\mathrm{A}})$ exists near two 'end' positions is considered, only the case in figure 39(c) is satisfied. If this condition disappears, only the case in figure 38(a) with the boundary of ω at the unvaried sign is suitable. On the other hand, the asymmetric wavy shape of $z = 0.7$ and 2.7 in figure 23(b) indicates that the two cases in figures 38(b) and 39(b) could exist mainly in the 'middle' region, e.g. $1.71 < z < 3.7$ in figure 23(b). Therefore, the spanwise waviness in the ω isosurfaces is mainly determined by the modulus of 5 with $\lambda_{\mathrm{DA}} = \frac{1}{5}L_{\mathrm{Z}}$ coupled with the weak modulus of 4 with $\lambda_{\mathrm{DA}} = \frac{1}{4}L_{\mathrm{Z}}$, as shown in figure 40. The moduli of 3 and 6 could appear locally near specific positions at a certain time. Typically, the asymmetric 'V'-like waviness can be well described by the superposition in figure 40(b) with the condition $\mathrm{sgn}(\omega) = -\mathrm{sgn}(\omega_{\mathrm{A}})$ near $z = 0$ and 2, while the asymmetrical 'W'-like wavy shape can be explained by the superposition in figure 40(c) with the condition of ω with the unvaried sign near $z = 0$ and 2.

Finally, figure 41 shows that the relative magnitude $(a_{\mathrm{DA}}/a_{\mathrm{A}})$ of ω_{DA} should reach at least 0.3 once the specific condition, i.e. $\mathrm{sgn}(\omega_{\mathrm{DA}}) = +\mathrm{sgn}(\omega) = -\mathrm{sgn}(\omega_{\mathrm{A}})$ near the 'end' position, e.g. $z = 2$, is satisfied. Furthermore, this specific condition indicates that ω_{DA} with the sign opposite to the sign of ω_{A} first appears near $z = 2$, where ω_{A} is weak enough (almost zero).

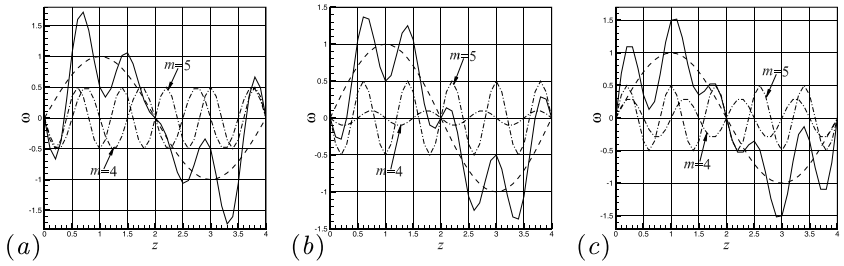

Figure 40. Amplitudes of ω, $\omega_{\rm A}$ with $a_{\rm A}=1$ and $\omega_{\rm DA}$ with two moduli (a) $a_{\rm DA}=-0.5$ $(m=4)$ and $a_{\rm DA}=-0.5$ $(m=5)$, (b) $a_{\rm DA}=-0.1$ $(m=4)$ and $a_{\rm DA}=-0.5$ $(m=5)$, and (c) $a_{\rm DA}=0.3$ $(m=4)$ and $a_{\rm DA}=0.5$ $(m=5)$, along the spanwise direction, where solid lines (—), dashed lines $(-\ -\ -)$ and dotted-dash lines $(-\cdot-)$ denote ω, $\omega_{\rm A}$ and $\omega_{\rm DA}$, respectively.

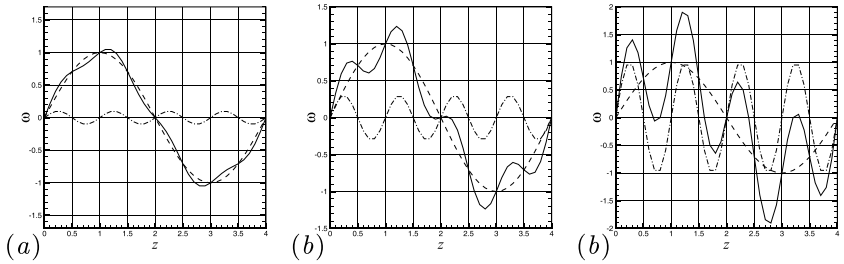

Figure 41. Amplitudes of ω, $\omega_{\rm A}$ with $a_{\rm A}=1$ and $\omega_{\rm DA}$ with (a) $a_{\rm DA}=0.1$, (b) $a_{\rm DA}=0.3$ and (c) $a_{\rm DA}=1$ along the spanwise direction with the modulus of $m=4$, where solid lines (—), dashed lines $(-\ -\ -)$ and dotted-dash lines $(-\cdot-)$ denote ω, $\omega_{\rm A}$ and $\omega_{\rm DA}$, respectively.

ORCID iD

L M Lin https://orcid.org/0000-0001-8933-9630

References

Agbaglah G and Mavriplis C 2017 Computational analysis of physical mechanisms at the onset of three-dimensionality in the wake of a square cylinder *J. Fluid Mech.* **833** 631–47

Agbaglah G and Mavriplis C 2019 Three-dimensional wakes behind cylinders of square and circular cross-section: early and long-time dynamics *J. Fluid Mech.* **870** 419–32

Barkely D and Henderson R D 1996 Three-dimensional Floquet stability analysis of the wake of a circular cylinder *J. Fluid Mech.* **322** 215–41

Barkley D, Tuckerman L S and Golubitsky M 2000 Bifurcation theory for three-dimensional flow in the wake of a circular cylinder *Phys. Rev.* E **61** 5247–52

Brede M, Eckelmann H and Rockwell D 1996 On secondary vortices in the cylinder wake *Phys. Fluids* **8** 2117–24

Darekar R M and Sherwin S J 2001 Flow past a square-section cylinder with a wavy stagnation face *J. Fluid Mech.* **426** 263–95

Henderson R D 1997 Nonlinear dynamics and pattern formation in turbulent wake transition *J. Fluid Mech.* **352** 65–112

Jiang H Y, Cheng L and An H W 2018 Three-dimensional wake transition of a square cylinder *J. Fluid Mech.* **842** 102–27

Jiang H and Cheng L 2019 Transition to the secondary vortex street in the wake of a circular cylinder *J. Fluid Mech.* **867** 691–722
Jiang H, Cheng L, Draper S and An H 2017 Prediction of the secondary wake instability of a circular cylinder with direct numerical simulation *Comput. Fluids* **149** 172–80
Jiang H, Cheng L, Draper S, An H and Tong F 2016 Three-dimensional direct numerical simulation of wake transitions of a circular cylinder *J. Fluid Mech.* **801** 353–91
Karniadakis G E and Triantafyllou G S 1992 Triantafyllou, Three-dimensional dynamics and transition to turbulence in the wake of bluff bodies *J. Fluid Mech.* **238** 1–30
Kokash H and Agbaglah G G 2022 On the origin of mode B instability of the wake of a square cylinder *Phys. Fluids* **34** 074116
Leweke T and Williamson C H K 1998 Three-dimensional instabilities in wake transition *Eur. J. Mech.* B **17** 571–86
Lin L M 2020 Vorticity sign law in three-dimensional wake of bluff body at low Reynolds number *Acta Phys. Sin.* **69** 034701 (in Chinese)
Lin L M 2022 Initially generated pure mode A in the three-dimensional wake transition of a circular cylinder *Fluid Dyn. Res.* **54** 035504
Lin L M 2023 Phase transition between pure modes A and B in a circular cylinder's wake. Part I: analysis of fluid forces *Fluid Dyn. Res.* **55** 035502
Lin L M, Shi S Y and Wu Y X 2018a Intrinsic relationship of vorticity between modes A and B in the wake of a bluff body *Theor. Appl. Mech. Lett.* **8** 320–5
Lin L M, Shi S Y and Wu Y X 2019 Physcial mechanism for origin of streamwise vortices in mode A of a square-section cylinder *Acta Mech. Sin.* **35** 411–8
Lin L M, Shi S Y, Zhong X F and Wu Y X 2019 Mechanism of wavy vortex and sign laws in flow past a bluff body: vortex-induced vortex *Acta Mech. Sin.* **35** 1–14
Lin L M and Tan Z R 2019 DNS in evolution of vorticity and sign relationship in wake transition of a circular cylinder: (pure) mode A *Acta Mech. Sin.* **35** 1131–49
Lin L M and Tan Z R 2022 DNS of the spatiotemporal evolution of the vorticity in (pure) mode B of a circular cylinder's wake *Fluid Dyn. Res.* **54** 015511
Lin L M and Wu Y X 2022 Theoretical analysis of vorticity in a hairpin vortex in the viscous sublayer of a laminar boundary layer *Eur. J. Mech.* B **94** 106–20
Lin L M, Zhong X F and Wu Y X 2018b Effect of perforation on flow past a conic cylinder at $Re = 100$: wavy vortex and sign laws *Acta Mech. Sin.* **34** 812–29
Ling G C and Chang Y 1999 Three-dimensional stability analysis of the periodic wake behind a circular cylinder by low-dimensional Galerkin method *Chin. J. Theor. Appl. Mech.* **31** 652–60
Luo S C, Chew Y T and Ng Y T 2003 Characteristics of square cylinder wake transition flows *Phys. Fluids* **15** 2549–59
Meiburg E and Lasheras J C 1988 Experimental and numerical investigation of the three-dimensional transition in plane wakes *J. Fluid Mech.* **190** 1–37
Persillon A and Braza M 1998 Physical analysis of the transition to turbulence in the wake of a circular cylinder by three-dimensional Navier-Stokes simulation *J. Fluid Mech.* **365** 23–88
Posdziech O and Grundmann R 2001 Numerical simulation of the flow around an infinitely long circular cylinder in the transition regime *Theor. Comput. Fluid Dyn.* **15** 121–41
Prasad A and Williamson C H K 1997 Three-dimensional effects in turbulent bluff-body wakes *J. Fluid Mech.* **343** 235–65
Rao A, Thompson M C, Leweke T and Hourigan K 2013 The flow past a circular cylinder translating at different heights above a wall *J. Fluids Struct.* **41** 9–21
Robichaux J, Balachandar S and Vanka S P 1999 Three-dimensional Floquet instability analysis of the wake of square cylinder *Phys. Fluids* **11** 560–78
Sheard G J, Thompson M C and Hourigan K 2003 A coupled Landau model describing the Strouhal-Reynolds number profile of a three-dimensional circular cylinder wake *Phys. Fluids* **15** L68–71
Thompson M C, Leweke T and Williamson C H K 2001 The physical mechanism of transition in bluff body wakes *J. Fluids Struct.* **15** 607–16
Williamson C H K 1996a Vortex dynamics in the cylinder wake *Annu. Rev. Fluid Mech.* **28** 477–539
Williamson C H K 1996b Three-dimensional wake transition *J. Fluid Mech.* **328** 345–407
Wu Z B and Ling G C 1993 Numerical study on the mechanism for three-dimensional evolution of vortex and the structural features in the wake behind a circular cylinder *Chin. J. Theor. Appl. Mech.* **25** 264–75

Yokoi Y and Kamemoto K 1992 Initial stage of a three-dimensional vortex structure existing in a two-dimensional boundary layer separation flow (Observation of laminar boundary layer separation over a circular cylinder by flow visualization *JSME Int. J. Ser.* II **35** 189–95
Yokoi Y and Kamemoto K 1993 Initial stage of a three-dimensional vortex structure existing in a two-dimensional boundary layer separation flow: visual observation of laminar boundary layer separation over a circular cylinder from the side of a separated region *JSME Int. J. Ser.* B **36** 201–6